



Year: 2021

Inhibited vertical mixing and seasonal persistence of a thin cyanobacterial layer in a stratified lake

Fernández Castro, Bieito ; Sepúlveda Steiner, Oscar ; Knapp, Deborah ; Posch, Thomas ; Bouffard, Damien ; Wüest, Alfred

Abstract: Harmful blooms of the filamentous cyanobacteria *Planktothrix rubescens* have become common in many lakes as they have recovered from eutrophication over the last decades. These cyanobacteria, capable of regulating their vertical position, often flourish at the thermocline to form a deep chlorophyll maximum. In Lake Zurich (Switzerland), they accumulate during stratified season (May–October) as a persistent metalimnetic thin layer (2 m wide). This study investigated the role of turbulent mixing in springtime layer formation, its persistence over the summer, and its breakdown in autumn. We characterised seasonal variation of turbulence in Lake Zurich with four surveys conducted in April, July and October of 2018 and September of 2019. Surveys included microstructure profiles and high-resolution mooring measurements. In July and October, the thin layer occurred within a strong thermocline (s) and withstood significant turbulence, observed as turbulent kinetic energy dissipation rates ($W\ kg$). Vertical turbulent overturns –monitored by the Thorpe scale– went mostly undetected and on average fell below those estimated by the Ozmidov scale (cm). Consistently, vertical diffusivity was close to molecular values, indicating negligible turbulent fluxes. This reduced metalimnetic mixing explains the persistence of the thin layer, which disappears with the deepening of the surface mixed layer in autumn. Bi-weekly temperature profiles in 2018 and a nighttime microstructure sampling in September 2019 showed that nighttime convection serves as the main mechanism driving the breakdown of the cyanobacterial layer in autumn. These results highlight the importance of light winds and convective mixing in the seasonal cycling of *P. rubescens* communities within a strongly stratified medium-sized lake.

DOI: <https://doi.org/10.1007/s00027-021-00785-9>

Posted at the Zurich Open Repository and Archive, University of Zurich

ZORA URL: <https://doi.org/10.5167/uzh-202052>

Journal Article

Published Version



The following work is licensed under a Creative Commons: Attribution 4.0 International (CC BY 4.0) License.

Originally published at:

Fernández Castro, Bieito; Sepúlveda Steiner, Oscar; Knapp, Deborah; Posch, Thomas; Bouffard, Damien; Wüest, Alfred (2021). Inhibited vertical mixing and seasonal persistence of a thin cyanobacterial layer in a stratified lake. *Aquatic Sciences*, 83:38.

DOI: <https://doi.org/10.1007/s00027-021-00785-9>

RESEARCH ARTICLE



Inhibited vertical mixing and seasonal persistence of a thin cyanobacterial layer in a stratified lake

Bieito Fernández Castro^{1,2} · Oscar Sepúlveda Steiner¹ · Deborah Knapp³ · Thomas Posch³ · Damien Bouffard⁴ · Alfred Wüest^{1,4}

Received: 27 January 2021 / Accepted: 1 February 2021
© The Author(s) 2021

Abstract

Harmful blooms of the filamentous cyanobacteria *Planktothrix rubescens* have become common in many lakes as they have recovered from eutrophication over the last decades. These cyanobacteria, capable of regulating their vertical position, often flourish at the thermocline to form a deep chlorophyll maximum. In Lake Zurich (Switzerland), they accumulate during stratified season (May–October) as a persistent metalimnetic thin layer (~2 m wide). This study investigated the role of turbulent mixing in springtime layer formation, its persistence over the summer, and its breakdown in autumn. We characterised seasonal variation of turbulence in Lake Zurich with four surveys conducted in April, July and October of 2018 and September of 2019. Surveys included microstructure profiles and high-resolution mooring measurements. In July and October, the thin layer occurred within a strong thermocline ($N \gtrsim 0.05 \text{ s}^{-1}$) and withstood significant turbulence, observed as turbulent kinetic energy dissipation rates ($\varepsilon \approx 10^{-8} \text{ W kg}^{-1}$). Vertical turbulent overturns –monitored by the Thorpe scale– went mostly undetected and on average fell below those estimated by the Ozmidov scale ($L_O \approx 1 \text{ cm}$). Consistently, vertical diffusivity was close to molecular values, indicating negligible turbulent fluxes. This reduced metalimnetic mixing explains the persistence of the thin layer, which disappears with the deepening of the surface mixed layer in autumn. Bi-weekly temperature profiles in 2018 and a nighttime microstructure sampling in September 2019 showed that nighttime convection serves as the main mechanism driving the breakdown of the cyanobacterial layer in autumn. These results highlight the importance of light winds and convective mixing in the seasonal cycling of *P. rubescens* communities within a strongly stratified medium-sized lake.

Keywords Microstructure turbulence · Metalimnion · Mixing · Lake Zurich · Mixing efficiency · Thin plankton layer · *Planktothrix rubescens* · Convection

Introduction

Temperate lakes are density-stratified throughout most of their annual cycle (Boehrer and Schultze 2008). During the stratified period, the water column typically assumes a vertical density structure consisting of three layers. These include a warmer surface layer (epilimnion) and a colder, weakly stratified deep layer (hypolimnion) separated by a region of continuous density stratification (metalimnion or thermocline). Stable conditions and the balance between nutrient and light availability, which exhibit opposing vertical distributions, make the thermocline an ecological niche for certain planktonic microbial organisms (Abbott et al. 1984; Sharples et al. 2001). These conditions often give rise to a sub-surface chlorophyll maximum of variable thickness. These may span less than a few meters and are termed thin

✉ Bieito Fernández Castro
bieito.fernandezcastro@epfl.ch;
b.fernandez-castro@soton.ac.uk

¹ Physics of Aquatic Systems Laboratory, Margaretha Kamprad Chair, Institute of Environmental Engineering, École Polytechnique Fédérale de Lausanne, Lausanne, Switzerland

² Present Address: Ocean and Earth Science, University of Southampton, Southampton, UK

³ Limnological Station, Department of Plant and Microbial Biology, University of Zurich, Seestrasse 187, Kilchberg, Zurich, Switzerland

⁴ Eawag, Surface Waters-Research and Management, Swiss Federal Institute of Aquatic Science and Technology, Kastanienbaum, Switzerland

layers in oceanographic literature (Dekshenieks et al. 2001; Sullivan et al. 2010; Durham and Stocker 2012). Thin layers have received growing attention in the scientific community due to their complex roles as ecological niches (Benoit-Bird et al. 2009), and because they often host harmful microbial communities (Nielsen et al. 1990; Broullón et al. 2020).

Efforts to reestablish oligotrophic conditions in some lakes has led to the proliferation of the harmful filamentous cyanobacterium *Planktothrix rubescens*, an unintended side-effect which poses a risk to human health (Jacquet et al. 2005; Ernst et al. 2009; Marti et al. 2016). In Lake Zurich (Switzerland), *P. rubescens* has become the dominant phytoplanktonic species over the last 40 years as the lake has recovered from strong eutrophication during the 1970s (Posch et al. 2012). *Planktothrix rubescens*' adaptation to low light and their capacity to control their vertical position via buoyancy regulation with gas vesicles (Walsby and Schanz 2002; Walsby 2005) allow them to proliferate in a metalimnetic thin layer that persists throughout the entire stratified season (May–October; Posch et al. 2012). This layer differs from other deep chlorophyll maxima in lakes due to the former's reduced thickness (< 2 m, Leach et al. 2018) and from similar structures in the ocean due to its temporal persistence (~6 months). Marine thin layers typically last for a few hours to a few days (Dekshenieks et al. 2001; Durham and Stocker 2012), by which time advection or turbulent mixing typically disrupt the layers (Steinbuck et al. 2009; Shroyer et al. 2014).

The few turbulence measurements available for marine thin layers indicate that turbulent mixing plays a critical role in regulating their formation and persistence (McManus et al. 2003; Cheriton et al. 2009; Steinbuck et al. 2009). Due to the scarcity of turbulence measurements in the presence of deep chlorophyll maxima in lakes however, the behaviour and scales of lacustrine thin layers is often inferred only from stratification (Leach et al. 2018). In Lake Zurich, for example, long-term persistence of *P. rubescens* is attributed to the strengthening and deepening of the metalimnion and to the increased duration of seasonal stratification (Yankova et al. 2016). Both of these sets of factors arise from warming experienced over the last decades (Livingstone 2003; Schmid and Köster 2016). However, different stratification regimes alone cannot explain the high abundance of *P. rubescens* in certain lakes (Jacquet et al. 2005). An adequate characterisation of turbulent mixing and its influence on *P. rubescens* communities can further constrain physical factors influencing their residence in Lake Zurich and similar systems.

Mixing in the metalimnion of lakes depends on the dissipation of internal waves (Lorke et al. 2005; Preusse et al. 2010) and turbulence originating at the surface, either by wind-driven shear (Imberger 1985; Pernica et al. 2014) or cooling-induced convection (Serra et al. 2007; Tedford et al. 2014). Previous turbulence measurements in the interior of

lakes during the stratified season revealed weak levels of internal mixing away from lake boundaries (Saggio and Imberger 2001; Etemad-Shahidi and Imberger 2001). This factor may explain the long-lasting layer persistence but turbulence is highly episodic and modulated by highly variable wind forcing (Saggio and Imberger 2001). Seasonal and higher-frequency variability in turbulent mixing may regulate formation of the *P. rubescens* thin layer in spring, its persistence over summer and breakdown in autumn, however, evidence for these mechanisms remains lacking.

To fill this gap in understanding, we conducted four field surveys in Lake Zurich in April, July and October of 2018, and in September of 2019. Surveys included microstructure profiles and high-resolution measurements of velocity and temperature fluctuations to characterise the seasonal and short-term variability of turbulent mixing in the metalimnion and its influence on the *P. rubescens* thin layer. Biophysical data collected during bi-weekly monitoring was used to interpret the high-resolution turbulence measurements. Comparison of Lake Zurich results with those from a similar lake (Lake Geneva) identified key physical factors that contribute to the proliferation of *P. rubescens* in some lakes but not in others.

Methods

Study site and sampling overview

Lower Lake Zurich is a long (28 km), narrow (3.8 km), deep (max. depth 136 m), and medium-sized (65 km²) perialpine lake. The lake is monomictic meaning that it experiences one seasonal deep convective mixing occasionally reaching the lake bottom in February–March, and subsequent thermal stratification during summer. Lake Zurich is exposed to light winds mainly from the northwest (mean \pm SD of 2.6 ± 1.8 m s⁻¹ for 2018), flowing along the main lake axis (Baracchini et al. 2019; Fig. S1).

Three surveys were carried out in order to investigate the seasonal variations in mixing conditions. Surveys occurred on 24–26 April, 17–19 July and 2–4 October 2018 at station st1 (120 m local water depth), located in Lower Lake Zurich, ~3 km from its deepest location (Fig. S1). During these surveys, we collected profile data with microstructure probes (Table S1), while a mooring system collected high-resolution current and temperature time-series within the thermocline (Table S2). We used hydrographic and biological data collected at the deepest point of the lake (st0, Fig. S1) as part of a long-term monitoring program to facilitate data interpretation over a broader seasonal context. An additional microstructure survey was conducted on 24–25 September 2019 to assess the role of nighttime convection for the seasonal breakdown of the *P. rubescens* layer.

Microstructure turbulence measurements

Microstructure profiles were collected with three different loose-tethered microstructure profilers deployed at st1 (2018) and st0 (2019). These included a SCAMP (Self-Contained Autonomous Microstructure Profiler, Precision Measurement Engineering) deployed in April 2018, a RSI VMP-500 (Vertical Microstructure Profiler, Rockland Scientific International) deployed in July and October 2018, and a RSI microCTD deployed in September 2019 (Table S1).

The three instruments were equipped with two FP07 thermistors that measure temperature fluctuations at a resolution of 10^{-5} °C and with a response time of $\tau \approx 10$ ms (Sommer et al. 2013). The FP07 thermistors sampled at a frequency of 100 Hz (SCAMP) and 512 Hz (VMP and microCTD). Additionally, lower-resolution high-accuracy temperature-conductivity-depth (CTD) and fluorescence sensors were mounted on all three microstructure profilers. Chlorophyll-*a* (chl-*a*) concentrations were derived from the latter. Lake water salinity and density (ρ) were calculated from the *in situ* temperature and conductivity measurements using lake-specific equations (Wüest et al. 1996). The buoyancy of the instruments was regulated to achieve a free-falling profiling speed of 10 to 20 cm s⁻¹ (SCAMP and VMP) and 30 to 40 cm s⁻¹ (microCTD). SCAMP and VMP were operated in free-falling mode, while the microCTD was operated alternatively in free-falling and free-rising mode, between the surface and 30 m depth.

The dissipation rate of thermal variance was calculated as

$$\chi = 6\kappa_T \left\langle \left(\frac{\partial T'}{\partial z} \right)^2 \right\rangle \quad [\text{K}^2 \text{ s}^{-1}], \quad (1)$$

where $\kappa_T = 1.4 \times 10^{-7} \text{ m}^2 \text{ s}^{-1}$ is the molecular diffusivity of heat. The Batchelor wavenumber (k_B) was calculated from fitting the power spectra from the vertical temperature gradient data to the Kraichnan spectrum (Kraichnan 1968) using the maximum likelihood method, which explicitly considers the noise curve of the thermistors (Ruddick et al. 2000). The rate of turbulent kinetic energy (TKE) dissipation (ϵ) was determined from the Batchelor wavenumber, $k_B = \frac{1}{2\pi} (\epsilon \nu^{-1} \kappa_T^{-2})^{1/4}$ [cpm]. These quantities were calculated over partially overlapping 1 m segments spaced at 25 cm.

Bad fits were discarded according to the misfit criteria proposed in Ruddick et al. (2000). The estimation of ϵ also requires consideration thermistor spatial resolution *vis a vis* the sensor's time-response. Although this effect was corrected with a single-pole function (Nash et al. 1999), the results can be highly uncertain for high ϵ values, when temperature fluctuations are expected at large wavenumbers. For a single pole correction and frequencies higher than the inverse of the time response $f_\tau = 1/\tau$ [Hz], the

spectral correction exceeds $\sim 60\%$. Taking into account the speed of descent for different instruments and the sensor time-response, f_τ corresponds to wavenumbers of ~ 670 cpm and ~ 280 cpm, for SCAMP/VMP and microCTD probes, respectively. This would equate to $\epsilon \approx 6 \times 10^{-6} \text{ W kg}^{-1}$ and $\sim 2 \times 10^{-7} \text{ W kg}^{-1}$. We interpret these values to represent safe upper limits for the detection of dissipation rates with the SCAMP/VMP and microCTD sensors. Cable strumming can cause perturbations of the descending profiler. These can result in extreme overestimation of dissipation rates during VMP sampling. Spikes interpreted to be cable strumming were removed. Similarly, due to limitations in microCTD performance during ascent when operated from a small boat under moderate winds, lower parts of profiles were often contaminated. These values were also removed.

Water column stability was characterised with the buoyancy frequency, N , defined as $N^2 = -g/\rho(\partial\rho/\partial z)$, where g is gravitational acceleration. The vertical turbulent heat diffusivity was calculated using the Osborn and Cox (1972) model given by:

$$K_T = \frac{\chi}{2(\partial\bar{T}/\partial z)^2} \quad [\text{m}^2 \text{ s}^{-1}]. \quad (2)$$

This equation expresses the fact that turbulence stirs the large-scale temperature gradient and thereby transfers variance to small scales where it is dissipated at a rate χ . This boosts the action of molecular diffusion and increases the rate of mixing.

The vertical scale of turbulent overturns was estimated using the Thorpe length-scale, $L_T = \sqrt{\langle d'^2 \rangle}$, where d' are the Thorpe displacements, i.e. the distance that a fluid parcel needs to be displaced in order to obtain a monotonic, stable density profile (Thorpe 1977; Lorke and Wüest 2002). Other relevant length-scales for turbulence are the Ozmidov ($L_O = (\epsilon N^{-3})^{1/2}$) and the Kolmogorov scales ($L_K = (\nu^3 \epsilon^{-1})^{1/4}$), at which inertial forces enter into equilibrium with buoyancy and viscosity, respectively. The ratios of these length-scales, i.e., buoyancy Reynolds number ($Re_b = (L_O/L_K)^{4/3} = \epsilon \nu^{-1} N^{-2}$) and the turbulent Froude number ($Fr_T = (L_O/L_T)^{2/3}$), are used to characterise the balance of forces and development of turbulence, and are related to the mixing efficiency (Ivey and Imberger 1991).

High-resolution mooring

A high-resolution (HR) mooring (Sepúlveda Steiner et al. 2021; see Fig. S1) was deployed within the thermocline (~ 12 m depth) at station st1 to characterise velocity and temperature fluctuations within the thin layer and its surroundings (Table S2). The mooring consisted of two fins. Five RBR temperature loggers sampling at 2 Hz were installed at different depths along the upper fin. The

second fin held a Nortek Aquadopp HR profiler (2 MHz) installed facing upwards for measuring current velocities at 1 Hz. The Aquadopp profiled 2.06 m divided into 104 bins of 0.02 m size along beams in a 25° orientation relative to vertical that covered the approximate vertical range of the temperature measurements. The HR-mooring was deployed for periods of several hours during several days in April, July and October 2018 close to st1 (Fig. S1). Due to operational issues such as vibrations along the mooring, some deployments generated only poor data. For this research, we analysed the July and October datasets that contained data of sufficient quality (Table S2).

Time-mean ENU (eastward–northward–upward or $u-v-w$) velocities were extracted by low-pass filtering at a cutoff period of 5 mins, which corresponds to about two times the local buoyancy period ($2\pi/N$), and by rotating the measured along-beam current velocities into ENU coordinates. TKE dissipation rates (ϵ) were estimated using the structure function method directly applied to along-beam velocities as described in Wiles et al. (2006). For this calculation we used 1024 point half-overlapping segments, corresponding roughly to 17 mins.

FluoroProbe and CTD profiles

As part of a long-term monitoring program, bi-weekly profiles ($n = 25$) of temperature, *P. rubescens* chl-*a* and other variables were measured near the deepest location of the lake at st0 (Fig. S1) between 10 January and 12 December 2018 with a TS-16–12 FluoroProbe (bbe Moldaenke GmbH, Kronshagen, Germany). Additionally, during the convection-oriented sampling in September 2019, 11 FluoroProbe casts were performed between 14:00 on the 24th and 10:40 on the 25th of September 2019.

Meteorological data

Hourly values for meteorological variables were obtained from the COSMO-1 (COnsortium of Small-scale MOdeling) weather model run by the Swiss Federal Office of Meteorology and Climatology (MeteoSwiss) covering the Swiss territory with a horizontal resolution of 1.1 km. Data was extracted for the grid-bin closest to st0. Heat fluxes through the lake surface (including shortwave and longwave radiation, as well as latent and sensible fluxes) were calculated following the derivation of Fink et al. (2014). Hourly surface water temperatures required for this calculation were interpolated from observations.

Analysis of basin-scale stability and mixing

Water column stability was quantified as the negative value of the background potential energy, i.e. the amount of mechanical energy that would be required to remove the existing stratification and fully mix the water column:

$$Sc = -\frac{1}{A_0} \int_{z_{max}}^{0m} g(\rho(z) - \bar{\rho})(z - z_c)A(z) dz \quad [\text{J m}^{-2}], \quad (3)$$

where $\bar{\rho}$ is the volume-averaged water density, $A(z)$ is the lake area at depth z (where z is defined as positive upwards and zero at the surface), $A_0 = A(0)$ is the surface area, z_{max} is the maximum depth of the lake and z_c is the depth of the lake's volume centroid. Lake bathymetry was obtained through the Swiss Federal Office of Topography (<https://www.swisstopo.admin.ch/>).

The potential of wind forcing to overcome the restoring effect of stratification, disturb the metalimnion and produce diapycnal mixing was quantified as the lake number, L_N (Imberger and Patterson 1989; Robertson and Imberger 1994):

$$L_N = \frac{A_0 Sc (1 - z_{TH}/z_{max})}{\rho_*^2 A_0^{1.5} (1 - z_c/z_{max})}, \quad (4)$$

where z_{TH} is the thermocline depth and $u_* = (\tau/\rho)^{1/2}$ is the friction velocity. Here, $\tau = \rho_{air} C_{10} W_{10}^2$ is the wind stress, where W_{10} is the wind speed 10 m above the lake surface, C_{10} is the wind drag coefficient, calculated according to Wüest and Lorke (2003), and ρ_{air} is the air density. Bi-weekly values of Sc were interpolated into hourly values to match the resolution of wind data for this calculation. The relative importance of sub-surface convective and wind mixing was quantified at 1-h intervals with the Monin–Obukhov length-scale, $L_{MO} = u_*^3/(\kappa B_0)$, where $\kappa = 0.41$ is the von Karman constant and B_0 is the surface buoyancy flux. Basin-scale vertical heat diffusivity (K_T^{BS}) was calculated with the heat-budget method (Powell and Jassby 1974) for hypolimnetic layers, and using a shear and convective velocity scaling for the surface boundary layer. Supplementary Text 1 describes these methods in detail.

Results

Seasonal stratification and *P. rubescens* thin layer

Figure 1 shows the evolution of atmospheric forcing and lake temperature at the monitoring station (st0) for Lake Zurich in 2018. From January to March, the lake lost heat to the atmosphere (Fig. 1a). The water column was weakly stratified in January and the surface mixed layer (SML, defined as the

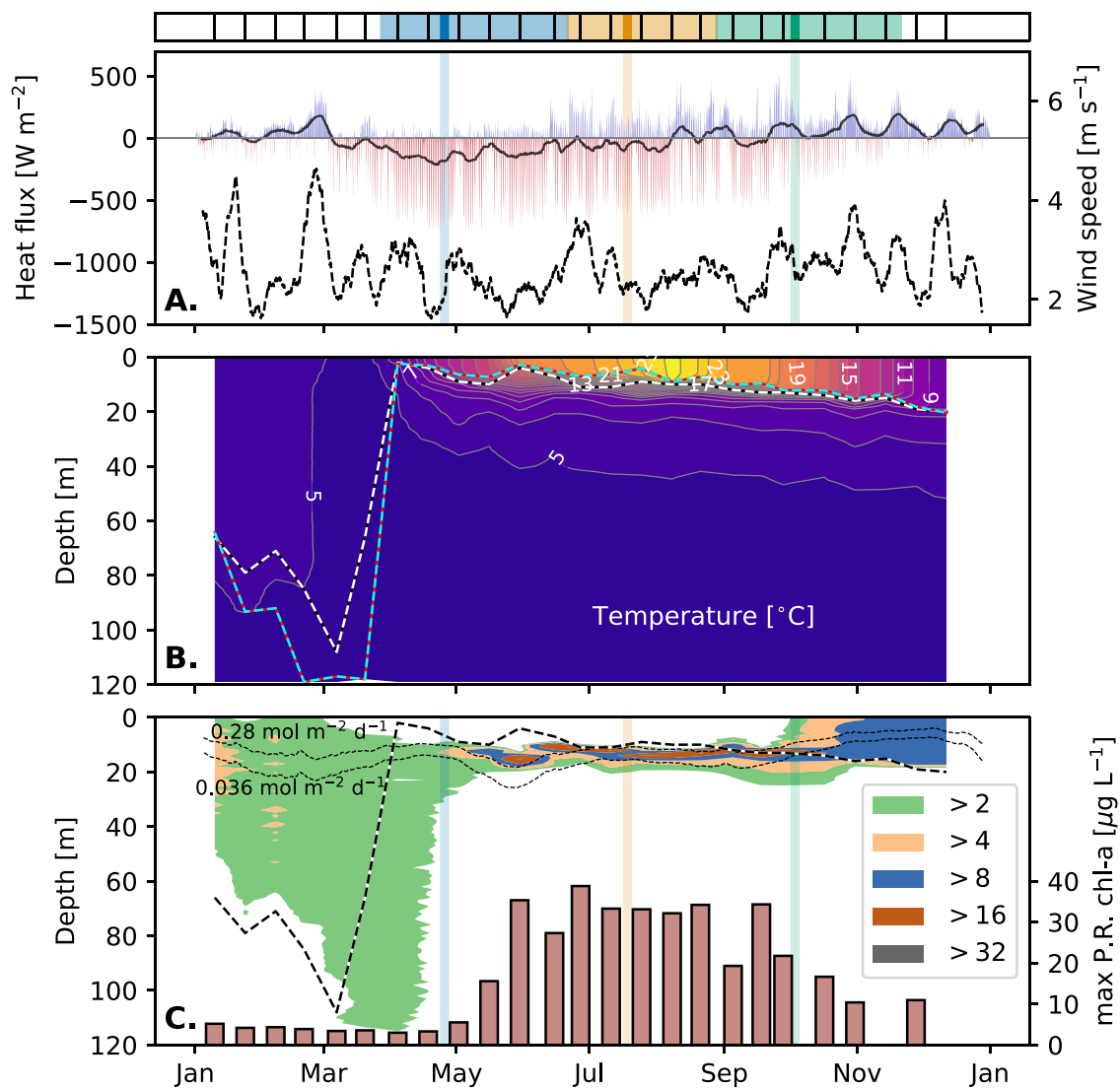


Fig. 1 Seasonal time-series of atmospheric and hydrographic conditions, and *P. rubescens* chl-a concentration in Lake Zurich during 2018. **a** Hourly (red-blue filling) and weekly mean (black) net heat flux between the lake and the atmosphere (positive upwards) and weekly mean wind speed (dashed) derived from the meteorological COSMO model; **b** vertical distribution of water temperature; and **c** vertical distribution of *P. rubescens* chl-a concentration ($\mu\text{g L}^{-1}$) (contours) and maximum concentration (bars). In **b**, **c**, the black-white thick dashed line represents the depth of thermocline (maximum temperature gradient) and the cyan-red tick dashed line, the surface mixed-layer (SML) depth. In **c**, the dotted thin lines rep-

resent the daily PAR fluxes resulting in *P. rubescens* neutral buoyancy ($0.28 \text{ mol photon m}^{-2} \text{ d}^{-1}$) and zero net growth ($0.36 \text{ mol photon m}^{-2} \text{ d}^{-1}$) (Walsby et al. 2004). Above the upper panel, vertical lines represent the sampling dates and the color shading represents the different stages of the seasonal evolution of *P. rubescens* thin layer from growth and settling during spring (blue: 20 March to 30 May), maximum stable concentration in early-mid summer (orange: 17 June to 8 August) to decline in late-summer and autumn (green: 21 August–31 October). Turbulence-oriented surveys are highlighted with darker shading (color figure online)

depth where temperature was 0.5°C lower than the near-surface value) deepened progressively. This continued until full mixing by mid-March (Fig. 1b) following a 10-day period of significant heat loss and relatively strong winds. The holomixis period was short with solar radiation dominating the heat budget after mid-March. As a result, a weak shallow thermocline had already developed by early April. Thereafter, surface temperature and water column stratification progressively increased to 26.5°C , as observed on 8 August.

During this warming period, a strong thermocline, with a temperature gradient ranging between 1.0 and $3.0^{\circ}\text{C m}^{-1}$, occurred just below the SML and showed a deepening trend from 2 to 10 m depth. Net cooling prevailed from August onwards and SML temperatures progressively decreased. The SML deepened steadily from 10 to 20 m depth in December, but the maximum thermal stratification remained strong ($2\text{--}3^{\circ}\text{C m}^{-1}$) until the end of September. It then declined

gradually as the SML expanded through the deeper part of the metalimnion, which was more weakly stratified.

Planktothrix rubescens was observed throughout the SML as relatively low chl-*a* concentrations (chl-*a* < 4 $\mu\text{g L}^{-1}$) during the mixing period in winter and occurred throughout the water column after holomixis (Fig. 1c). From May onwards, *P. rubescens* communities formed a thin layer located within the main thermocline between 10 and 17 m depth. *Planktothrix rubescens* regulate their vertical position according to the daily dosages of photosynthetically available radiation (PAR; Walsby et al. 2004). The records described here found *P. rubescens* mostly located between daily PAR isolines for which *P. rubescens* acquires neutral buoyancy ($0.28 \text{ mol photon m}^{-2} \text{ d}^{-1}$) and for which the net growth becomes zero ($0.036 \text{ mol photon m}^{-2} \text{ d}^{-1}$; thin dashed lines in Fig. 1c; Walsby et al. 2004). The layer remained stable, with peak concentrations between 30 and 40 $\mu\text{g L}^{-1}$, until October, when the thermocline deepened and approached the layer. From mid-October, *P. rubescens* concentration in the SML began to increase but the peak persisted until the end of the month, when the thermocline transgressed the layer, and the latter dispersed.

For the rest of the year, the *P. rubescens* population was located exclusively in the SML at moderate concentrations of $\sim 10 \mu\text{g L}^{-1}$.

Microstructure measurements

Seasonal changes in stratification and mixing environment

Our turbulence sampling detected three stages in the seasonal development of the *P. rubescens* layer. The first microstructure and HR-mooring survey was carried out between 24 and 26 April 2018 (blue, Fig. 1), shortly before formation of the thin layer. The second survey occurred between 17 and 19 July (orange), when the thin layer had been established for more than 2 months and water column stability approached its maximum value. Finally, the third sampling took place between 2 and 4 October (green), when some *P. rubescens* chl-*a* had been detected in the SML but the chl-*a* peak remained sharp and well defined in spite of its reduced amplitude.

During the sampling in April, heating outpaced nighttime cooling and hourly wind speeds were maximal (6 m s^{-1}) on the 25th, such that no microstructure profiles could be

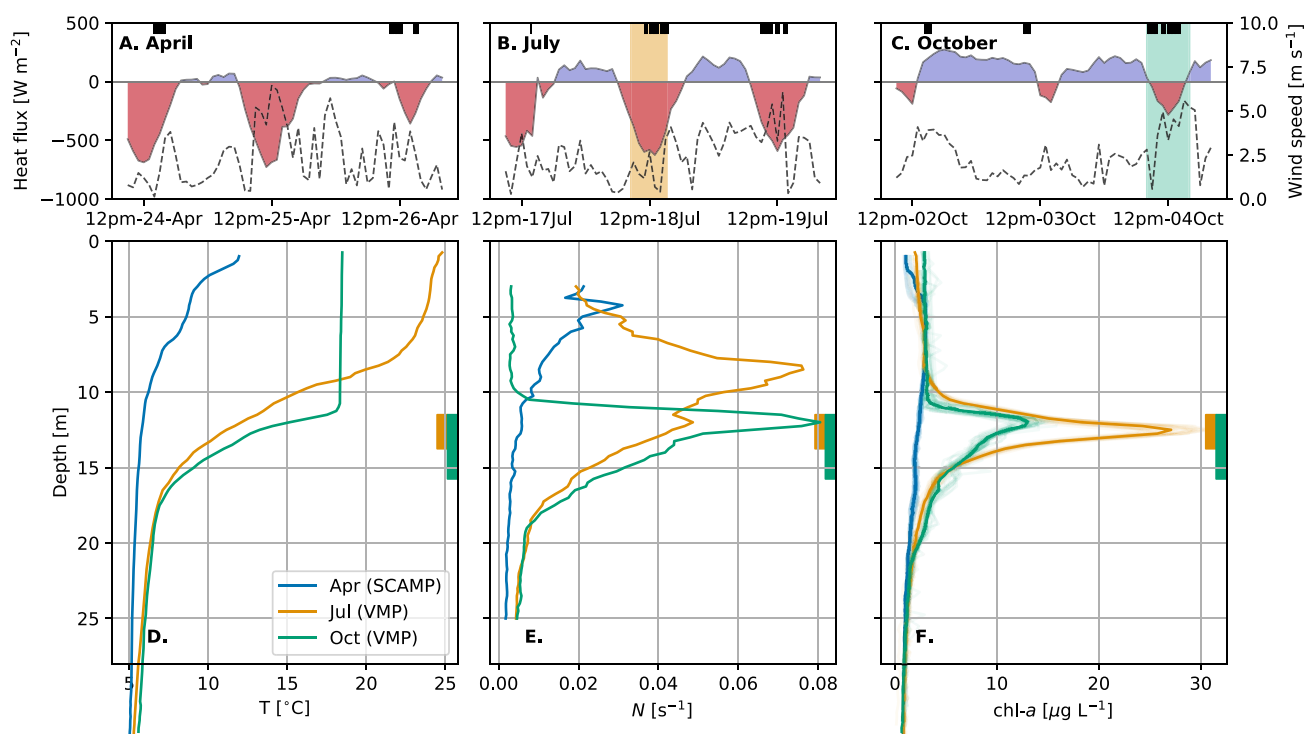


Fig. 2 Hourly meteorological conditions (net heat flux, blue-red filling; wind speed, dashed black) derived from the COSMO model during the 3 microstructure and mooring samplings in 2018: **a** 24–26 April 2018, **b** 17–19 July 2018, and **c** 2–4 October 2018. Median profiles of **d** temperature, **e** buoyancy frequency and **f** chl-*a* fluorescence derived from the microstructure profiles at st1 for April 2018 (blue, SCAMP profiler), July 2018 (orange, VMP profiler) and October 2018 (green, VMP profiler). In **a**–**c**, microstructure profiles are indi-

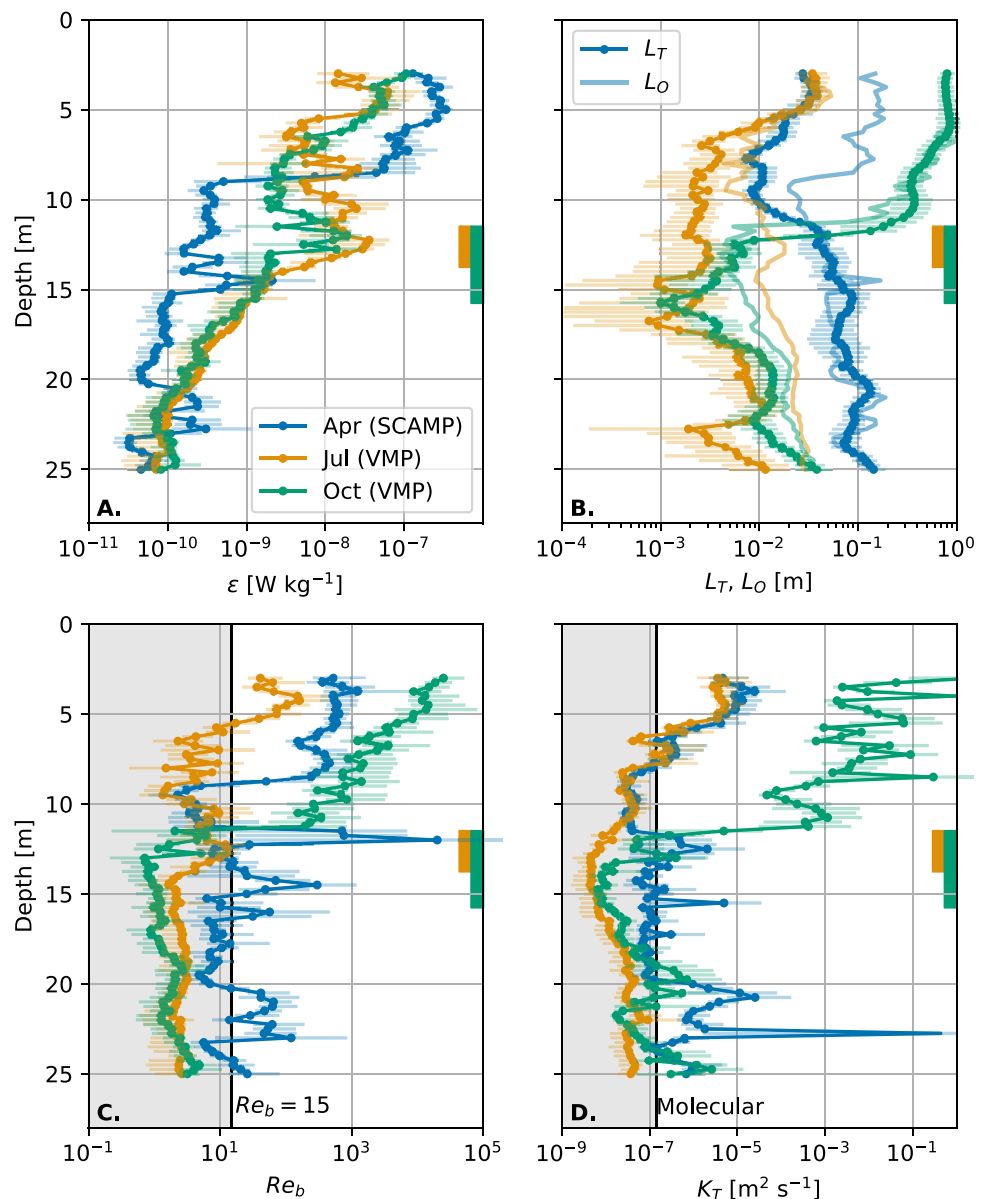
cated with black ticks, and the duration of mooring deployments is indicated with color filling. In panels **c**–**f** the depth range of the *P. rubescens* thin layer, defined as the range where chl-*a* is larger than an e-folding fraction of the maximum value ($\text{chl-}a > \max(\text{chl-}a)/e$), is indicated by filled rectangles for July (orange) and October (green). Individual profiles for chl-*a* are shown in **f** as semi-transparent lines. Individual profiles were projected onto isothermal coordinates to remove the effect of internal wave motions (color figure online)

carried out on that day. Except for this day, wind remained $< 4 \text{ m s}^{-1}$ (Fig. 2a). Thermal stratification was still moderate ($N_{\max} \approx 0.02 \text{ s}^{-1}$), with a shallow thermocline located above 5 m depth (Fig. 2d, e). Chl-*a* measured with the SCAMP was low ($< 5 \mu\text{g L}^{-1}$) and no thin layer was observed (Fig. 2f). In July, nighttime cooling intensified but daytime heating still dominated the net heat budget. Maximum wind speeds of $> 5 \text{ m s}^{-1}$ were observed on the 19th (Fig. 2b). The water column was thermally stratified from the surface ($N \approx 0.02 \text{ s}^{-1}$), and a strong thermocline extended from 7 to 17 m depth with maximum stratification ($N_{\max} = 0.075 \text{ s}^{-1}$) at 9 m depth (Fig. 2d, e). A $\sim 2 \text{ m}$ thick, vertically symmetric thin layer of chl-*a* (max. $30 \mu\text{g L}^{-1}$) occurred at 13 m, 4 m below the stratification maximum (Fig. 2f). In October, nighttime cooling was prominent and daytime heating

had weakened. The relatively low wind speeds (2 m s^{-1}), increased on 4 October (6 m s^{-1} , Fig. 2c). A homogeneous SML, not observed in the previous surveys, extended down to 10.5 m depth, and rested on an even sharper thermocline ($N_{\max} \approx 0.1 \text{ s}^{-1}$ at 11.5 m depth, Fig. 2d, e). A weaker chl-*a* maximum ($13 \mu\text{g L}^{-1}$) was observed at $\sim 12 \text{ m}$ depth coinciding with maximum N . The chl-*a* peak had broadened (4.5 m) to become asymmetric with a sharp upper edge (Fig. 2f).

April data gave elevated ε values of $2 \times 10^{-7} \text{ W kg}^{-1}$ in the upper 8 m. Below this depth, ε dropped sharply to very low values ($\leq 10^{-10} \text{ W kg}^{-1}$; Fig. 3a). In July and October, ε showed a similar vertical distribution, with larger values between 4×10^{-9} and $4 \times 10^{-8} \text{ W kg}^{-1}$ in the upper 14 m, and a second maximum in the depth range of the main

Fig. 3 Mean profiles of turbulence-related variables derived from the microstructure profiles during 24–26 April 2018 (blue, SCAMP profiler), 17–19 July 2018 (orange, VMP profiler) and 2–4 October 2018 (green, VMP profiler) at st1. **a** TKE dissipation rate (ε), **b** Thorpe (L_T , dotted lines) and Ozmidov (L_O , semi-transparent lines) length-scales, **c** buoyancy Reynolds number (Re_b), and **d** turbulent heat diffusivity (K_T). The 90% confidence intervals from bootstrap sampling are represented as faded horizontal lines. The depth range of the *P. rubescens* thin layer, defined as the range where chl-*a* is larger than an e-folding fraction of the maximum value ($\text{chl-}a > \max(\text{chl-}a)/e$), is indicated by filled rectangles for July (orange) and October (green) (color figure online)



thermocline (10–13 m). From the base of the main thermocline, ε decreased to 10^{-10} W kg $^{-1}$ at 25 m depth.

The Thorpe scale, L_T , describing the size of turbulent overturns, was 1–3 cm in the upper 10 m during April and gradually increased with depth to up to 10 cm at 20–25 m depth (Fig. 3b). In this deeper layer, L_T was similar to the Ozmidov scale (L_O), but L_O was 10 times larger than L_T in the upper 10 m. In July, L_T was ~ 3 cm in the upper 5 m but exhibited smaller thickness below ($L_T = 1$ mm to 1 cm). During this sampling, L_O was also about one order of magnitude larger than L_T throughout the water column. October data gave relatively large L_T and L_O values (10 cm to 1 m) that resembled each other in the upper 12 m. These declined sharply below 12 m to the order of ~ 1 cm with L_T being generally smaller than L_O .

April data gave a buoyancy Reynolds number of $Re_b > 100$ in the upper 8 m indicating energetic turbulence (Fig. 3c). At greater depths, $Re_b < 15$, except for a local peak at 12 m. Smaller values of $Re_b < 15$ indicate that turbulence is buoyancy-suppressed (Ivey and Imberger 1991; Bouffard and Boegman 2013). In July, Re_b exceeded 100 in the upper 5 m but declined rapidly below this depth to $Re_b < 15$ in deeper layers. October data showed a sharp transition for Re_b at 11 m depth from high values ($Re_b \approx 1000$) in the SML to molecular values within the thermocline.

The turbulent heat diffusivity (K_T in Eq. 2) followed the same vertical distributions as those exhibited by Re_b for the three sampling dates (Fig. 3d). K_T approached (April) or fell below (July, October) molecular levels in the depth range where $Re_b \lesssim 15$, including the metalimnion. April and July data gave

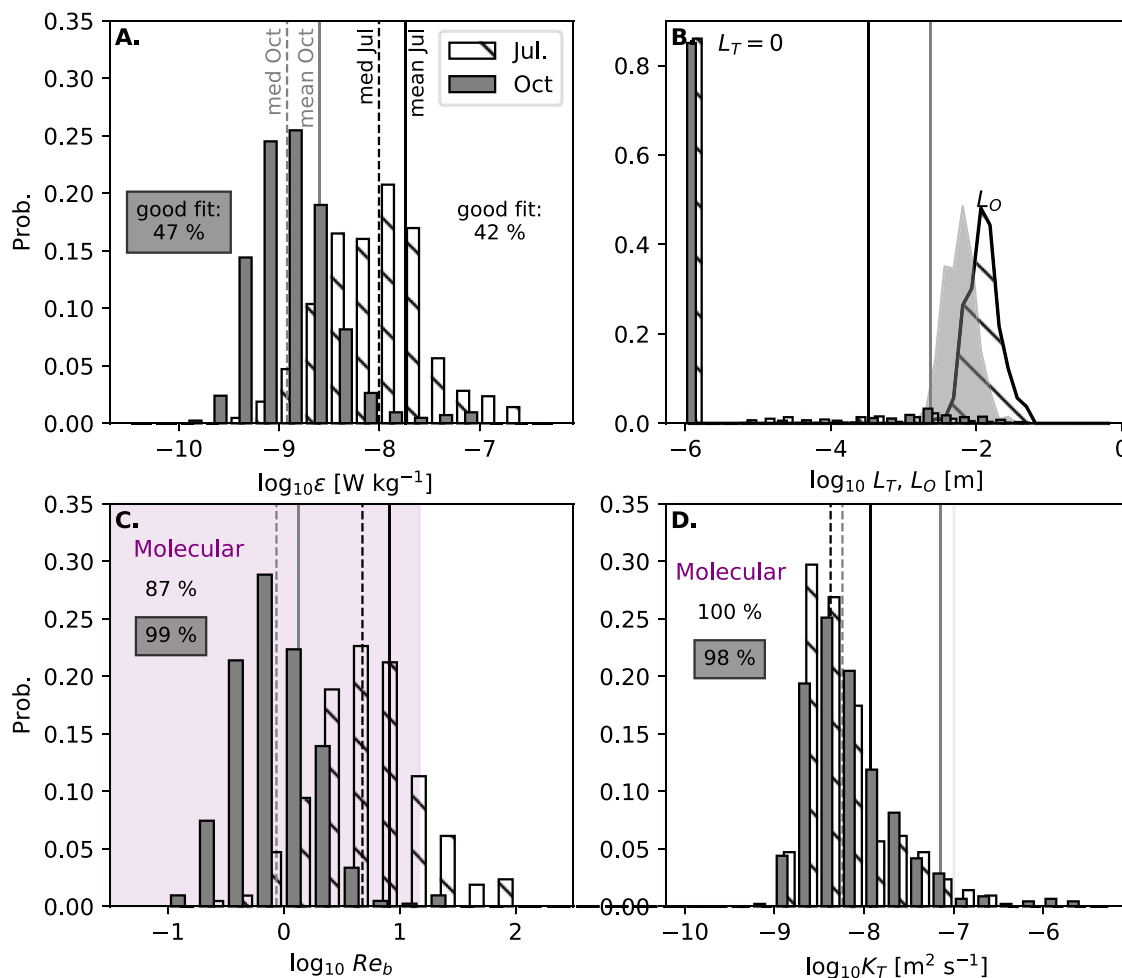


Fig. 4 Probability distribution of turbulence-related quantities within the *P. rubescens* layer, defined as the depth range where $\text{chl-}a > \max(\text{chl-}a)/e$, derived from the microstructure profiles during 17–19 July 2018 (white bars) and 2–4 October 2018 (grey bars) at st1. **a** TKE dissipation rate (ε), **b** Thorpe (L_T , bars) and Ozmidov (L_O , lines and filled patches) length-scales, **c** buoyancy Reynolds number (Re_b), and **d** turbulent heat diffusivity (K_T). Mean and median values are

represented by solid and dashed vertical lines, respectively (see values in Table 1). Black lines are for July and grey lines for October, respectively. The probability of occurrence of molecular conditions according to the criteria $Re_b < 15$ and $K_T \leq \kappa_T$ is indicated in **c**, **d**, respectively. For the quantities depending on fitting to the theoretical temperature-gradient spectrum (ε , Re_b , L_O , K_T), only good fits are shown (color figure online)

Table 1 Median and arithmetic mean values and 90%-confidence intervals (CI, in brackets) for the turbulence parameters in the *P. rubescens* thin layer during the July 2018 and October 2018 sam-

plings based on the data collected with the microstructure profiler (VMP) and the HR-mooring

	VMP		Mooring	
	Median	Mean [CI]	Median	Mean [CI]
July 2018				
Depth range [m]	11.75–14.25		10.84–12.90	
N [s^{-1}]	0.042	0.043 [0.025–0.043]	0.042	0.043 [0.042–0.043]
ϵ [10^{-8} W kg^{-1}]	0.99	1.8 [1.6–3.4]	0.91	1.4 [1.38–1.47]
L_O [cm]	1.25	1.4 [0.7–1.5]	1.08	1.18 [1.16–1.19]
L_T [cm]	0.05	0.23 [0.14–0.35]		
Re_b	4.8	8.2 [7.1–14.9]	3.6	5.0 [4.9–5.1]
K_T [10^{-7} m ² s ⁻¹]	0.04	0.12 [0.10–0.31]		
	VMP		Mooring	
	Median	Mean [CI]	Median	Mean [CI]
October 2018				
Depth range [m]	11.75–16		10.13–12.19, $T \leq 18^\circ C$	
N [s^{-1}]	0.042	0.052 [0.050–0.055]	0.072	0.071 [0.068–0.139]
ϵ [10^{-8} W kg^{-1}]	0.12	0.25 [0.21–0.78]	2.9	6.8 [6.3–7.3]
L_O [cm]	0.59	0.66 [0.31–0.68]	1.46	1.66 [1.62–1.69]
L_T [cm]	0.3	1.5 [0.7–2.8]		
Re_b	0.86	1.3 [1.2–2.8]	10	21 [19–23]
K_T [10^{-7} m ² s ⁻¹]	0.06	0.71 [0.39–7.38]		

Median and mean values of L_T were calculated by considering only detectable overturns ($L_T > 0$)

moderate K_T values (10^{-5} m² s⁻¹) in the upper ~ 7 m, while October data gave large values ($\sim 10^{-2}$ m² s⁻¹) in the SML.

Turbulence statistics in the plankton layer

Figure 4 and Table 1 show probability distributions and mean values for turbulence-related parameters derived from the microstructure profiles within the chl-*a* maximum during July and October 2018. The vertical extent of the layer was defined as the depth range where chl-*a* exceeded the e-folding fraction of the maximum (chl-*a* > max (chl-*a*)/*e*). This range should contain 85% of the layer biomass assuming a Gaussian distribution.

In July, energy dissipation rates ranged over three to four orders of magnitude (ϵ from 10^{-10} to 10^{-6} W kg^{-1}) within the depth range of the thin layer (11.75–14.25 m, Table 1; Fig. 4a). This parameter followed a lognormal distribution slightly skewed towards high values. As a consequence, the mean values for ϵ of $1.8 [1.6 - 3.4] \times 10^{-8}$ W kg^{-1} (90% confidence intervals in brackets) exceeded median values (0.99×10^{-8} W kg^{-1}). It is worth noting that only about 42% of the fits to the Kraichnan spectrum met the quality criteria. This indicates that the shape of the temperature gradient spectra was possibly influenced by fine structures under the strongly stratified conditions (Gregg 1977; Luketina

and Imberger 2001). In October, the ϵ distribution centered on smaller values (median 0.12×10^{-8} W kg^{-1} , mean $0.25 [0.21 - 0.78] \times 10^{-8}$ W kg^{-1}) but also exhibited a small number of outlying peaks of large values ($> 10^{-8}$ W kg^{-1}). These suggest a sharp vertical gradient for ϵ within the plankton layer (Fig. 3a). Nearly half of the fits (47%) from the October data failed to meet the goodness of fit criteria.

The Ozmidov length-scale (L_O) exhibited a tight symmetrical distribution for July and October with respective median values of 1.3 and 0.60 cm, and respective mean values of $1.4 [0.70 - 1.50]$ cm and $0.66 [0.31 - 0.68]$ (Table 1; Fig. 4b). However, L_T was 0 for ~90% of the datapoints indicating that overturning motions were undetectable (the median of L_T was zero in both samplings). When detectable, the Thorpe scale tended to fall below the Ozmidov scale, i.e., $L_T < L_O$. For typical overturns detected ($L_T > 0$) in July and October, L_T equaled $0.23 [0.14 - 0.35]$ cm and $1.5 [0.7 - 2.8]$ cm, respectively. The $\epsilon \approx 10^{-8}$ W kg^{-1} gives a Kolmogorov length-scale on the order of 3 mm. This estimate approaches the size of the detected overturns in July suggesting effective damping by viscous forces.

Within the thin layer, $Re_b < 15$ was found for 87% and 99% of the samples for July and October, respectively (Fig. 4c). July and October data gave median values of 4.8 and 0.86 and mean values of $8.2 [7.1 - 14.9]$, and $1.3 [1.2 - 2.8]$ indicating

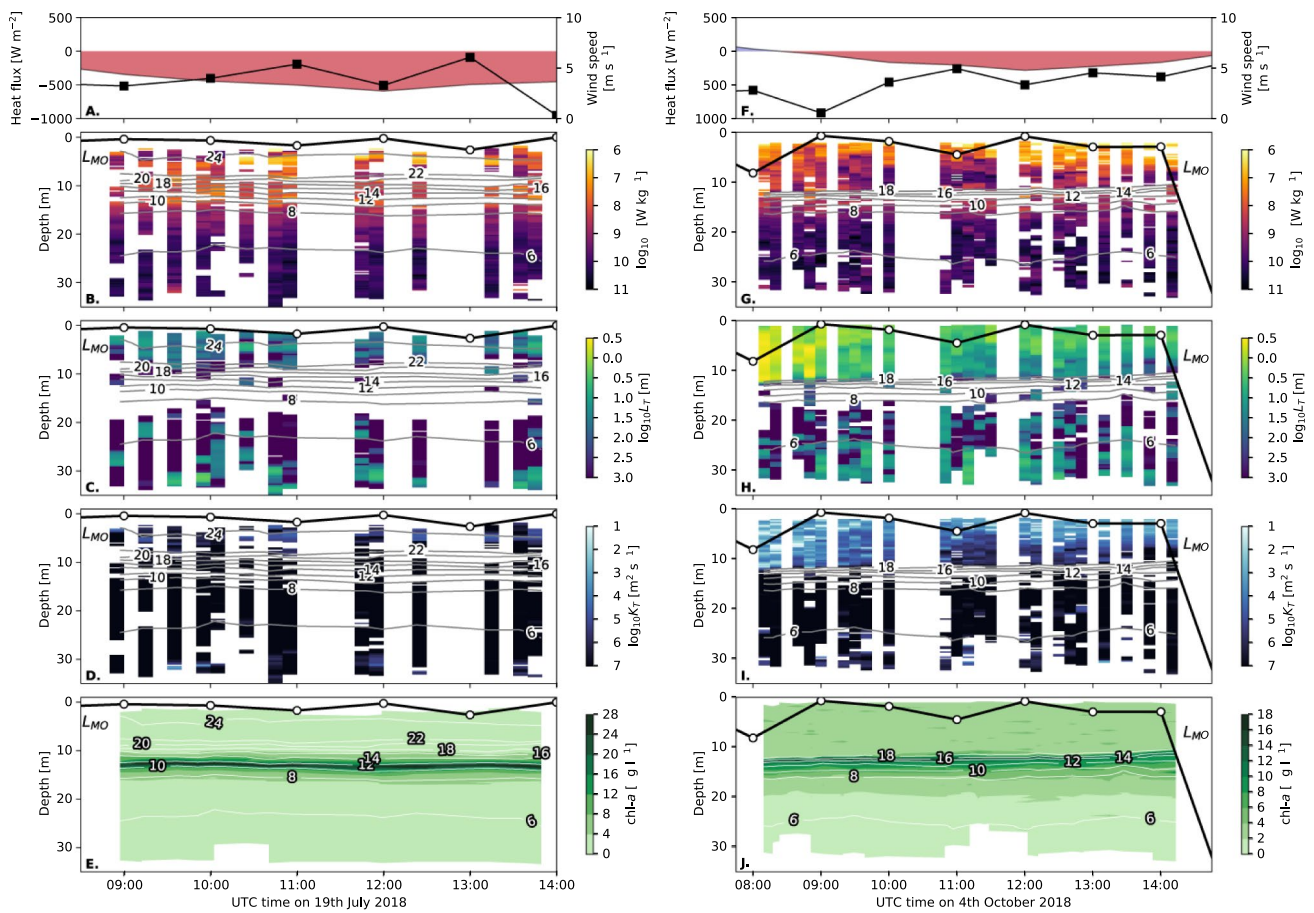


Fig. 5 Microstructure measurements collected with a VMP profiler during 19 July and 4 October 2018 at st1. **a, f** Hourly surface heat flux (colors) and wind speed (black) derived from COSMO model; **b, g** TKE dissipation rate (ϵ); **c, h** Thorpe scale (L_T); **d, i** heat dif-

fusivity (K_T); and **e, j** chl-*a*. Temperature contours every 2 °C and hourly values of the Monin–Obukhov length-scale (L_{MO} , black line with dots) are also shown in all panels except **a, f**. Time in the x-axis is UTC time (local time was UTC+2) (color figure online)

that non-turbulent, molecular fluxes prevailed. Estimated K_T distributions for July (median: $0.04 \times 10^{-7} \text{ m}^2 \text{ s}^{-1}$, mean: $0.12 [0.10 - 0.31] \times 10^{-7} \text{ m}^2 \text{ s}^{-1}$) and October (median: $0.06 \times 10^{-7} \text{ m}^2 \text{ s}^{-1}$, mean: $0.71 [0.39 - 7.40] \times 10^{-7} \text{ m}^2 \text{ s}^{-1}$) agreed with the former estimates indicating that turbulent mixing did not enhance molecular heat fluxes.²

Short-term variability

Microstructure profiles measured on a repeated basis established patterns of some short-term temporal variability in turbulence and chl-*a* profiles. Figure 5 shows this variability for the days of 19 July and 4 October, when winds reached relatively high speeds ($\sim 5 \text{ m s}^{-1}$, Fig. 5a, f). For the July date, the isotherms remained mostly flat during the 5 h of sampling (Fig. 5a–e) indicating weak internal wave activity. The *P. rubescens* layer persisted unperturbed between the 8 and 18 °C isotherms of the thermocline (Fig. 5e). Despite moderate wind speeds, the Monin–Obukhov length-scale (L_{MO}) characterising the penetration of wind mixing below

the surface remained shallow ($< 5 \text{ m}$) due to the stabilizing heat flux. The ϵ distribution showed little variation around the mean estimate for the profile (Fig. 5b; blank spaces represent rejected fits for the theoretical temperature-gradient spectrum). The upper 10 m showed some variability with turbulent patches having $\epsilon \approx 10^{-7} - 10^{-6} \text{ W kg}^{-1}$. The L_T record illustrates the scarcity and small size of overturns within the main thermocline (empty bins represent $L_T = 0$ in Fig. 5c). In the upper 10 m, estimates of $L_T \approx 10 \text{ cm}$ showed very little variation. Below 15 m depth, intermittent turbulent patches with $L_T \gtrsim 10 \text{ cm}$ occasionally appeared. Vertical diffusivity (Fig. 5d) approached or fell below molecular levels throughout the day except in the relatively turbulent patches of the upper SML, but none the turbulent patches reached the *P. rubescens* layer (Fig. 5d). The profiles collected on 18 July, a day of lower wind speeds, showed even weaker variability (Fig. S3).

Conditions varied more in October when early morning profiles captured the transition from nighttime cooling to daytime heating and wind speeds increased during

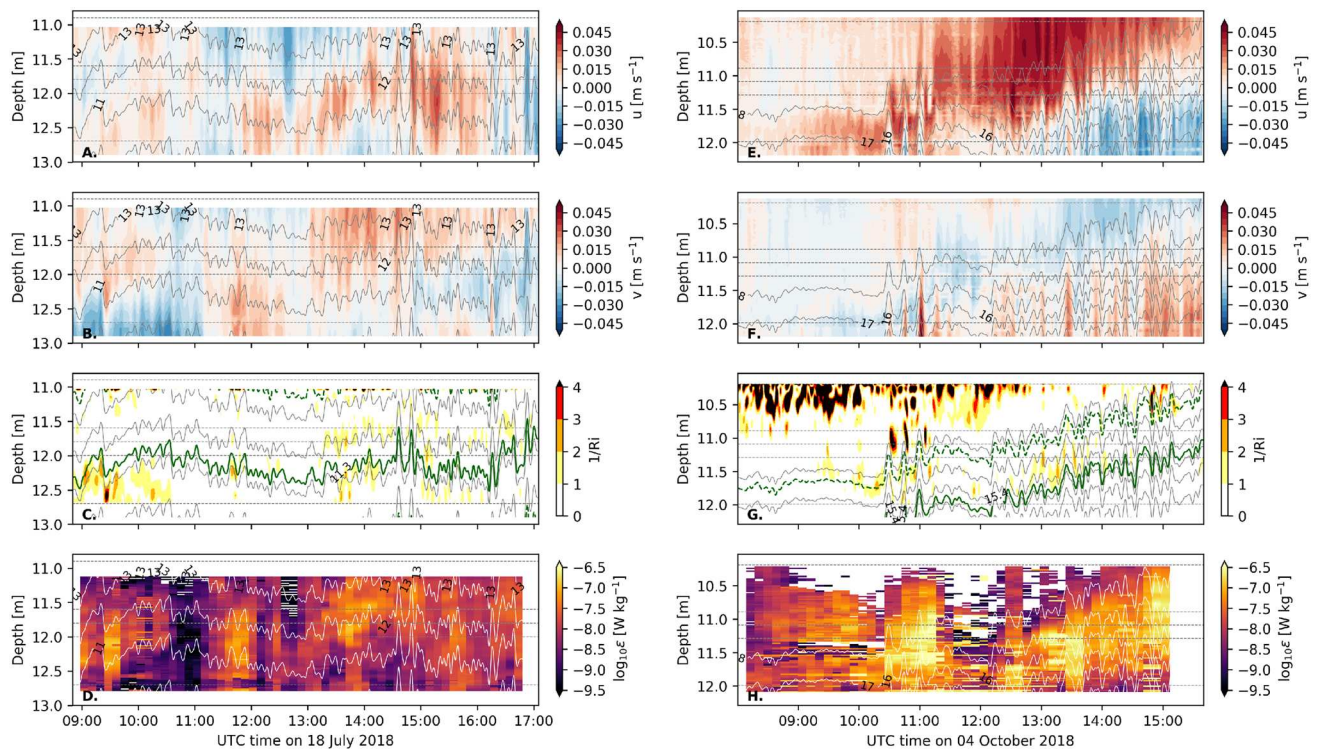


Fig. 6 Measurements of horizontal eastward (u) and northward (v) velocities (filled contours in **a**, **b**, **e**, **f**), temperature (grey lines in all panels), inverse Richardson number ($1/Ri = S^2/N^2$, **c**, **g**), and TKE dissipation rate (ϵ , **d**, **h**) obtained with the HR-mooring at st1 in July and October 2018. The position of the thermistors is indicated by horizontal dashed lines. Data on **a–d** were collected on 18 July 2018, and data on **e–h** correspond to 4 October 2018. The displayed

temperature and velocity signals were smoothed with a low-pass Butterworth filter with a 5-min period. Data in blank areas in **d**, **h** were excluded due to poor beam correlation (segment median correlation $< 70\%$). The isotherms corresponding to the mean location of chl- a maximum, and the upper and lower edges of the chl- a layer (e-folding fraction of the maximum value) are shown as green solid and dashed lines, respectively, in **c**, **g** (color figure online)

the morning (Fig. 5f). Over the 6 hours of sampling, the thermocline rose gradually by 2 m (Fig. 5g–j) indicating likely a basin-scale response to enhanced winds. The chl- a maximum appeared between the 8 and 18°C isotherms and tracked a stable upwards movement (Fig. 5j). Estimates of turbulence remained relatively uniform between the upper part of the SML and the top of the *P. rubescens* layer until 9am. These indicated moderate levels of mixing with $\epsilon \approx 10^{-8} - 10^{-7} \text{ W kg}^{-1}$, $K_T \approx 10^{-2} \text{ m}^2 \text{ s}^{-1}$ and large turbulent overturns $L_T > 1 \text{ m}$ (Fig. 5g–l). With the onset of warming, L_{MO} diminished ($< 5 \text{ m}$), overturns decreased ($L_T < 1 \text{ m}$) and ϵ and K_T declined, particularly in the lower part of the SML. As a result of the relatively strong winds, ϵ and K_T remained large in the upper SML down to 7–8 m depth. This daytime wind-driven sub-surface mixing however did not reach the thermocline or cyanobacterial layer.

High-resolution mooring observations within the thermocline

The high-resolution measurements by moored instruments revealed high-frequency internal wave variability not captured by the profilers. The patterns detected included cm-scale vertical internal wave-driven isothermal displacements and velocities on cm s^{-1} scales (Fig. 6). In July, the sampling range (10.84–12.9 m depth) spanned a region included in the main thermocline with a relatively uniform and pronounced temperature gradient (roughly 3.5 °C over 2.5 m; Fig. 6a, b). The overall amplitude of fluctuations in current velocities and isothermal displacements varied little during the 8-h deployment. In October, the sampling range (10.13–12.19 m depth) included part of the SML at the beginning of the deployment. Measurements detected only the upper, sharper edge of the *P. rubescens* layer, located between the 18°C and 15°C isotherms (Fig. 6e, f). For the first two hours, background currents were relatively weak with no fluctuations of the isotherms. After 10:30, current velocities increased gradually, and high-frequency fluctuations commenced. The intensification (up to a maximum of 5 cm s^{-1} at about 13:00)

coincided with an expansion of the pycnocline such that it occupied the whole sampling range by the end of the deployment. This event likely reflects rising winds that morning, which also appeared in the microstructure profiles.

Horizontal flow velocities documented vertical structure within a narrow, meter-scale range

during both deployments. The shear in the mean flow ($S^2 = (\partial u / \partial z)^2 + (\partial v / \partial z)^2$) can trigger shear instabilities to drive turbulence and mixing if it overcomes the stabilizing effect of stratification. This situation occurs when the gradient Richardson number ($Ri = N^2 / S^2$) falls below the critical value of 1/4 (Miles 1961). High-resolution

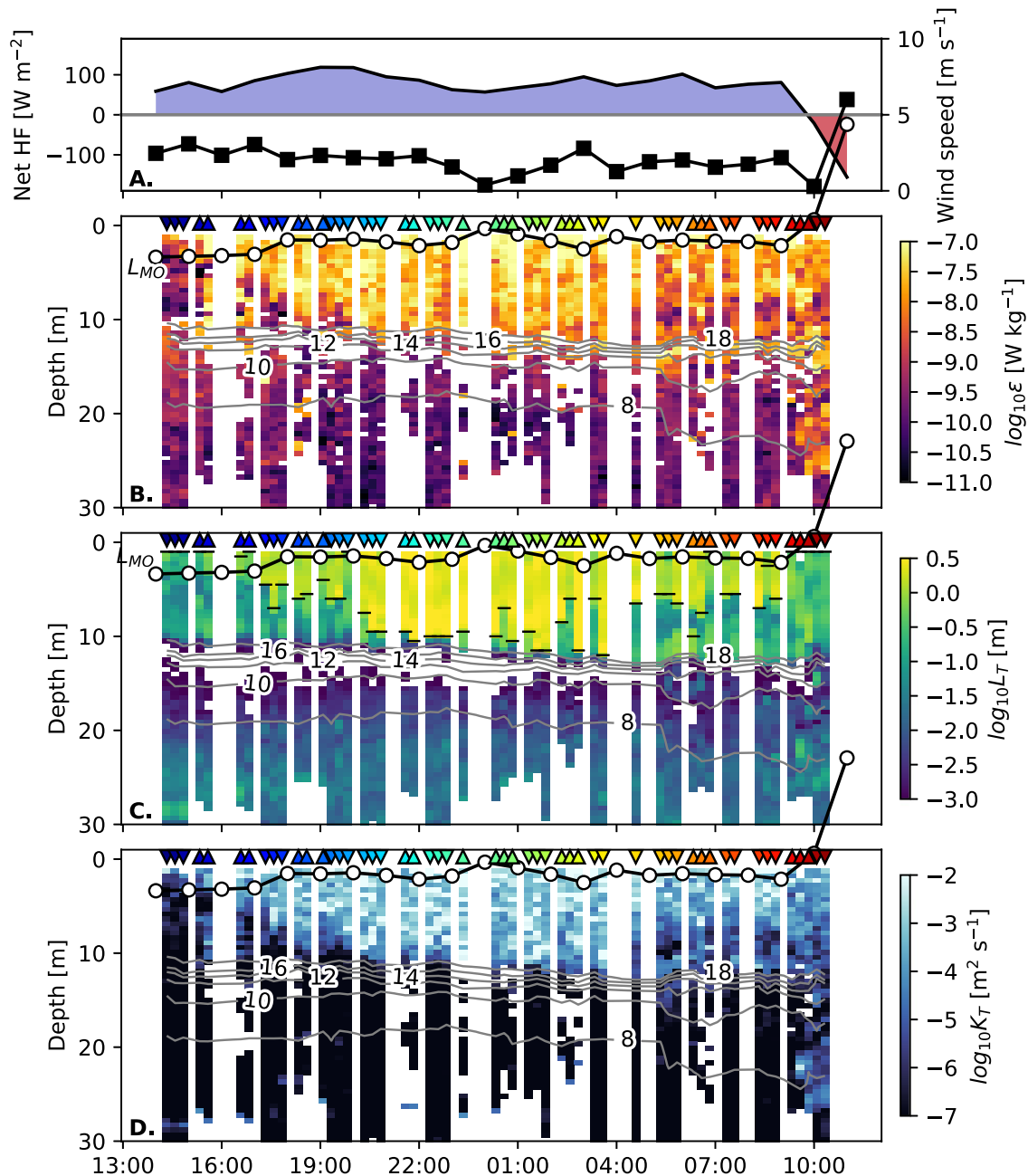


Fig. 7 Microstructure measurements collected with a microCTD profiler during the nighttime sampling on 24–25 September 2019 at st0. **a** Hourly surface heat flux (colors) and wind speed (black) derived from COSMO model, **b** TKE dissipation rate (ϵ), **c** Thorpe scale (L_T), and **d** heat diffusivity (K_T). Temperature contours every 2 °C and hourly values of the Monin–Obukhov length-scale (L_{MO} , black

line with dots) are plotted in **b–d**. Upward and downward looking triangles indicate ascending and descending profiling, respectively. The color scale of the triangles represents the sampling time. Surface mixing-layer depth (defined as $L_T > 1$ m) is indicated with horizontal black markers in **c**. Time in the x-axis UTC time (local time was UTC+2) (color figure online)

measurements show that, despite the existence of background shear, unstable Ri were not often obtained, due to the strong stratification. Specifically, conditions in July and October met stable criteria ($Ri > 1$) 88% and 80% of the time (Fig. 6c, g). Furthermore, most unstable values occurred in October within the weakly-stratified SML. These exerted little effect on the thermocline, where the *P. rubescens* layer occurred.

Energy dissipation rates derived from turbulent velocity fluctuations using structure functions ranged between 10^{-10} and 10^{-7} W kg $^{-1}$ in July and rose to values on the order of 10^{-10} – 10^{-6} W kg $^{-1}$ during October (Fig. 6d, h). In July, ϵ exhibited intermittent structure between calmer (from 10:30 to 11:00 and between 12:00 and 13:00) and more dissipative conditions. The periods of lower dissipation took place under conditions of reduced vertical shear when $Ri < 1$ events were not detected (Fig. 6c). In October, ϵ began with weak values during the first 2 h, when internal wave activity was weak and strengthened thereafter. The average ϵ was $1.4 [1.4 - 1.5] \times 10^{-8}$ W kg $^{-1}$ (median: 0.91×10^{-8}) and $6.8 [6.3 - 7.3] \times 10^{-8}$ W kg $^{-1}$ (median: 2.9×10^{-8}) for July and October, respectively. Table 1 lists these values as well as their respective ranges. The values in July showed very good agreement with microstructure estimates for the same depth range (Fig. 3a). Values derived for L_O and Re_b also resembled those derived from profile observations (Table 1). In October, high-resolution velocities gave somewhat larger values for ϵ , but, Re_b remained in the range indicating a molecular regime (mean 21 [19–23], median: 10).

Nighttime sampling: the role of convective mixing

The asymmetric vertical distribution of chl-*a* in October and enhanced turbulence during the early morning of 4 October 2018 (before solar heating outpaced heat lost) suggest that convective mixing in autumn could potentially disrupt the *P. rubescens* layer and cause the decline observed in the long-term data (Fig. 1). It was not possible to test this idea with the 2018 dataset, since daytime measurements do not capture layer dynamics during fully developed convective mixing.

To overcome this limitation, a nighttime survey was conducted with a microstructure profiler, a CTD and a FluoroProbe between 14:40 UTC (16:40 local) on 24 September 2019 and 10:40 on 25 September 2019 (Fig. 7). This field campaign occurred under conditions of low wind speeds (2 m s^{-1}) and moderate heat loss (Fig. 7a). Observations recorded a 10 m SML with $T = 18^\circ \text{C}$ and a sharp pycnocline between 10 and 15 m depth (Fig. 7b). Consistent with the previous results, data failed to provide good fits to the theoretical temperature-gradient spectrum for the thermocline. As a consequence, ϵ could not be determined in several instances (Fig. 7b). Turbulent overturns were rare (Fig. 7c), and vertical diffusivity approached or fell below molecular values (Fig. 7d). The SML, below the Monin-Obukhov depth gave initially low values for ϵ (10^{-10} W kg $^{-1}$) with $L_T < 1$ m and K_T approaching molecular scale. After 17:00, a mixing layer with enhanced ϵ (2×10^{-8} W kg $^{-1}$), $L_T (> 1 \text{ m})$ and $K_T (> 10^{-4} \text{ m}^2 \text{ s}^{-1})$ penetrated beneath L_{MO} . At about 21:00, the mixing reached the thermocline, which also deepened slightly overnight. The intensity and downward penetration of the convective mixing declined after 04:00 and completely ceased after sunrise when the heat flux was negative (into the lake).

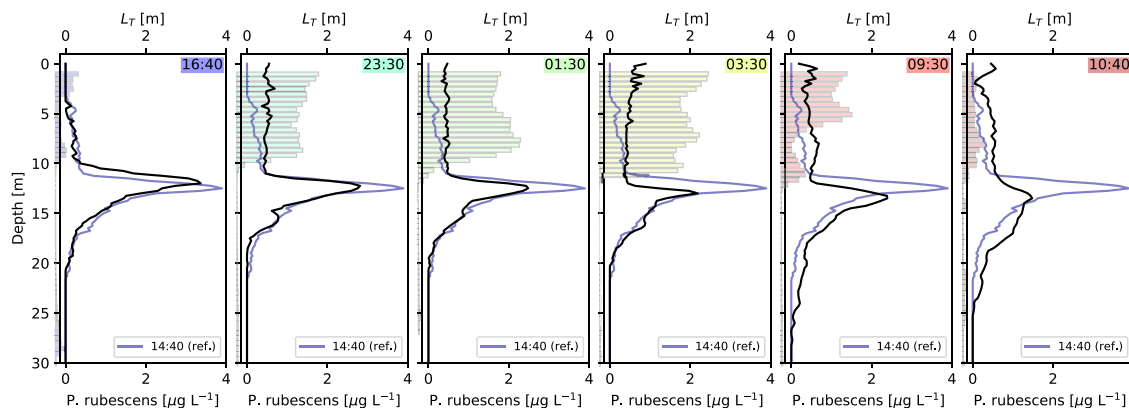


Fig. 8 Profiles of *P. rubescens* chl-*a* concentration collected during the nighttime sampling on 24–25 September 2019 at st0 with a FluoroProbe. The profile at the indicated sampling time (color rectangle) is shown as a black line, and initial reference profile collected at

14:40 is shown as a light blue line. The bars represent mean profiles of Thorpe scale (L_T) between the previous and current FluoroProbe profile. The color code indicates the sampling time in relation to Fig. 7 (color figure online)

Figure 8 shows effects of convective mixing on *P. rubescens* distribution as determined by the FluoroProbe measurements. The initial profiles in the early afternoon (14:40) are plotted in light blue in every panel for clarity, and bars representing the L_T are included to illustrate the vertical extent and intensity of mixing. *Planktothrix rubescens* appears as a well defined peak in the afternoon and at relatively low concentration in the SML. Overnight, convection reached the top of the thin layer. The maximum *P. rubescens* layer concentration progressively declined and the community's concentration in the SML increased due to filament entrainment by convective plumes eroding the layer from above. These results clearly show the disruptive effect of nighttime convection on the structure of the *P. rubescens* metalimnetic layer in early autumn.

Discussion

On the nature of suppressed thermocline mixing

Independent estimates of TKE dissipation with microstructure and high-resolution current measurements in the highly stratified seasonal thermocline of Lake Zurich revealed moderate levels of dissipation, $\epsilon \approx 10^{-8} \text{ W kg}^{-1}$. Dissipation exhibited a degree of intermittency spanning three orders of magnitude. The turbulent heat diffusivity, K_T , exhibited persistently small values of the order of $10^{-8} \text{ m}^2 \text{ s}^{-1}$. Their scale relative to the molecular heat diffusivity means that turbulent fluxes across the thermocline were negligible. These estimates indicate very limited mixing efficiency ($\Gamma = K_T N^2 / \epsilon \approx 0.002$) wherein most of the TKE is lost to viscous dissipation and does not produce mixing. Data also revealed infrequent unstable Richardson number values ($Ri < 1/4$) and vertical turbulent overturns ($\lesssim 10\%$ occurrence) within detection limits. Detected overturns were characterised by $L_T \leq L_O \approx 2 \text{ cm}$, which fell below typical values in the ocean thermocline (Gregg 1987) and even the lowest estimates from hypolimnetic observations in lakes (Etemad-Shahidi and Imberger 2001; Lorke and Wüest 2002). Vertical turbulent overturns store available potential energy, $0.5 L_T^2 N^2$ (Dillon and Park 1987), which is transferred to the mean density profile when overturns collapse. The scarcity of overturns and their small size thus provide strong indication of very weak turbulent mixing in the thermocline.

Different sources of evidence, including observations, laboratory experiments and simulations, indicate that turbulent fluxes become negligible when the buoyancy Reynolds number ($Re_b = (L_O/L_K)^{4/3}$), which measures of the size of the inertial subrange ($L_O > l > L_K$), falls below $\mathcal{O}(10 - 100)$ (Ivey and Imberger 1991; Gibson 1999; Shih et al. 2005). Our thermocline observations fall mostly

within this range and thus explain the relative weak mixing observed. Another parameter used to estimate mixing efficiency of turbulence is the turbulent Froude number, $Fr_T = (L_O/L_T)^{2/3}$. This parameter represents a ratio between the turbulent eddy size required to achieve an equilibrium between inertial and buoyancy forces (L_O) and the observed vertical eddy size (L_T). When Fr_T approaches or falls below one, turbulent eddies begin to disrupt background stratification, and the system experiences its maximum potential for turbulent mixing (Mashayek et al. 2017). Because L_T values fell far below L_O for our dataset on the Lake Zurich thermocline, Fr_T was very large. This means that the turbulent eddies were too small to disturb the background stratification. Instead, low mean values for Re_b and L_T (the latter sometimes close to the Kolmogorov scale) suggest strong dampening of turbulent motions by viscosity (Ivey and Imberger 1991). Such situations can produce only very weak turbulent fluxes, consistent with those appearing in the observations described here.

Overall, the results presented here comport with previous turbulence measurements in small and medium size lakes, which showed only very weak turbulent fluxes occurring in their interiors (Saggio and Imberger 2001; Etemad-Shahidi and Imberger 2001; Boegman et al. 2003; MacIntyre et al. 2009; Weck and Lorke 2017). Mixing at the basin-scale depends most strongly on processes occurring at the boundaries (Goudsmit et al. 1997; Wüest et al. 2000; MacIntyre et al. 1999). With direct measurements using eddy covariance, Etemad-Shahidi and Imberger (2001) and Saggio and Imberger (2001) quantified turbulent fluxes in the thermoclines of two stratified lakes. These researchers found similar situations to that described here for Lake Zurich, wherein high dissipation rates ($\epsilon \approx 10^{-7} \text{ W kg}^{-1}$) occurred only with small scale overturns and negligible vertical fluxes. The authors interpreted turbulent dissipation as driven by wave-wave interactions, which resulted in high-intermittency and weak vertical fluxes rather than formation of overturning billows due to shear instabilities (Itsweire et al. 1993; Teoh et al. 1997). Turbulence properties of the Lake Zurich metalimnion also resembled those reported in association with thin plankton layers in the ocean. These layers are frequently found within sharp thermoclines, where Re_b (McManus et al. 2003; Broullón et al. 2020) and vertical diffusivities (Steinbuck et al. 2009) are small ($Re_b < 100$ and $K_T \lesssim 10^{-6} \text{ m}^2 \text{ s}^{-1}$) suggesting weak vertical turbulent mixing.

Turbulence characterised by low Re_b and only occasional small scale overturns, suggests anisotropic turbulent motions. These conditions violate assumptions underlying methodologies used to calculate ϵ both from microstructure and high-resolution current measurements (Dillon and Caldwell 1980; Smyth and Moum 2000; Bluteau et al. 2011) such that the large ϵ values must be interpreted with caution.

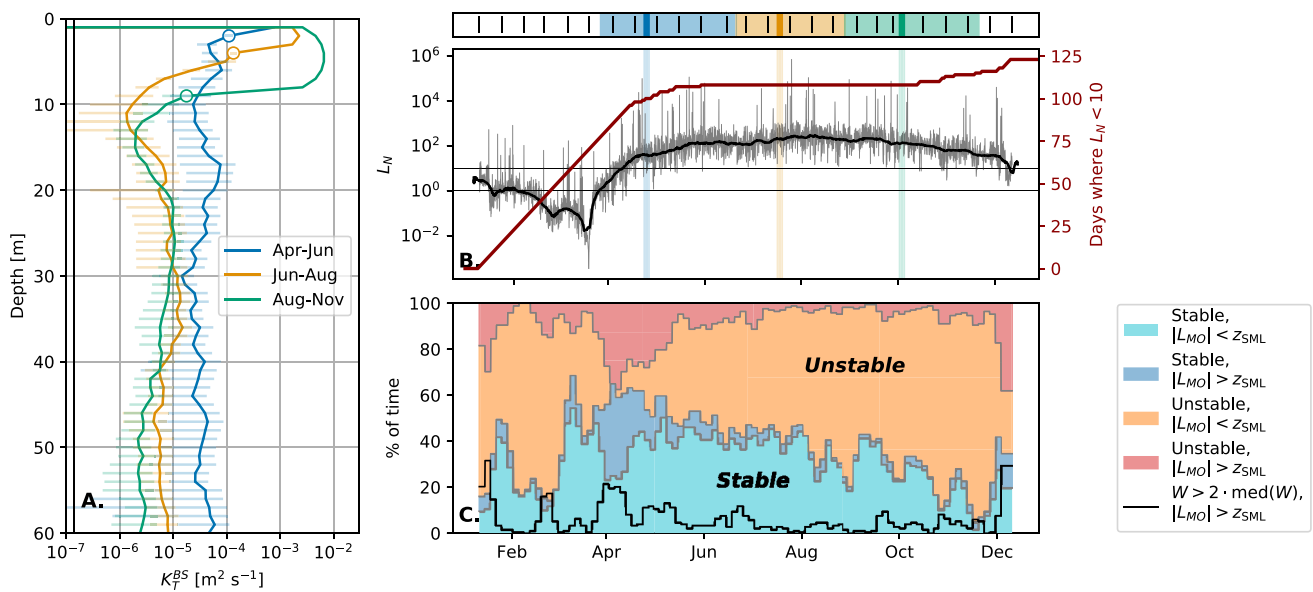


Fig. 9 **a** Basin-scale vertical heat diffusivity (K_T^{BS} ; derived from the heat budget method in the meta- and hypolimnetic layers, and from a boundary layer scaling in the SML) for the spring (blue: 20 March–30 May), mid-summer (orange: 17 June–8 August) and late-summer/autumn (green: 21 August–31 October) periods; **b** time-series of hourly (grey) and weekly (black) lake number (L_N) and cumulative counts of days when $L_N < 10$ during at least one hour (red);

and **c** weekly counts of convectively stable ($L_{MO} < 0$) and unstable ($L_{MO} > 0$) situations when the absolute value of L_{MO} is smaller/larger than the depth of the surface mixed-layer (z_{SML}). Dark-red and dark-blue filling indicate conditions favorable for wind-driven entrainment in the metalimnion ($|L_{MO}| > z_{SML}$). Counts of situations when strong winds (twice the median value) could cause entrainment ($|L_{MO}| > z_{SML}$) are shown as a thin back line. The mean SML depths are shown as circles in **a** (color figure online)

About half of the temperature-gradient spectral fits were discarded because the observational spectra did not follow the expected shape according to the established fit criteria. This indicates that conditions were possibly not turbulent in all cases, and fine-scale structures influenced the spectra (Gregg 1977). Dissipation rates derived from high-resolution velocities also depend on a multiplicative fit constant. Under unisotropic conditions, this could deviate from the prescribed isotropic value and generate uncertainties of $> 50\%$ in the estimates (Jabbari et al. 2016). Agreement between the two different methods and the consistency with previous observations allow for a certain degree of confidence in our results however. Substantial errors associated with ϵ estimates furthermore would not compromise first order interpretations of suppressed metalimnetic mixing.

Basin-scale mixing and thin layer persistence

In addition to its well known seasonal persistence, our high-resolution measurements revealed the exceptional stability of the *P. rubescens* thin layer at sub-daily scales (Fig. 5). This only abated when nighttime convective mixing penetrated into the layer during the September 2019 sampling. The persistence appears due to the reduced turbulent fluxes in the metalimnion. However, our sampling strategy may

have undersampled the effect of turbulent mixing on the *P. rubescens* thin layer for two reasons. First, the forcing conditions during the four surveys may not have captured the full range of weather variability. Second, the *P. rubescens* community occurs throughout the lake (Salcher et al. 2011; Garneau et al. 2015) including along slope and near-shore regions. As such, the likely effects of boundary mixing (Goudsmit et al. 1997) on the community would not appear in offshore observations like the ones conducted here.

To investigate the role of unresolved mixing, we used hourly meteorological data and bi-weekly water column observations to calculate the lake number (L_N). We also estimated a basin-scale turbulent diffusivity using the heat budget method and a surface boundary layer scaling (see Supplementary Text 1 for details) (Fig. 9). The lake number indicates the potential of wind stress to significantly disturb the metalimnion by driving upwelling and exciting internal motions. Significant disturbance occurs when $L_N < 10$. L_N exhibited values < 10 almost every day over the winter period until April (Fig. 9b). This indicates that wind forcing could easily overcome the existing weak stratification and drive turbulent mixing. From April, the number of days when $L_N < 10$ progressively declines such that no such days occurred in June and throughout the entire summer. This indicates strong damping of interior motions and mixing by stratification. Mixing events reappeared from October

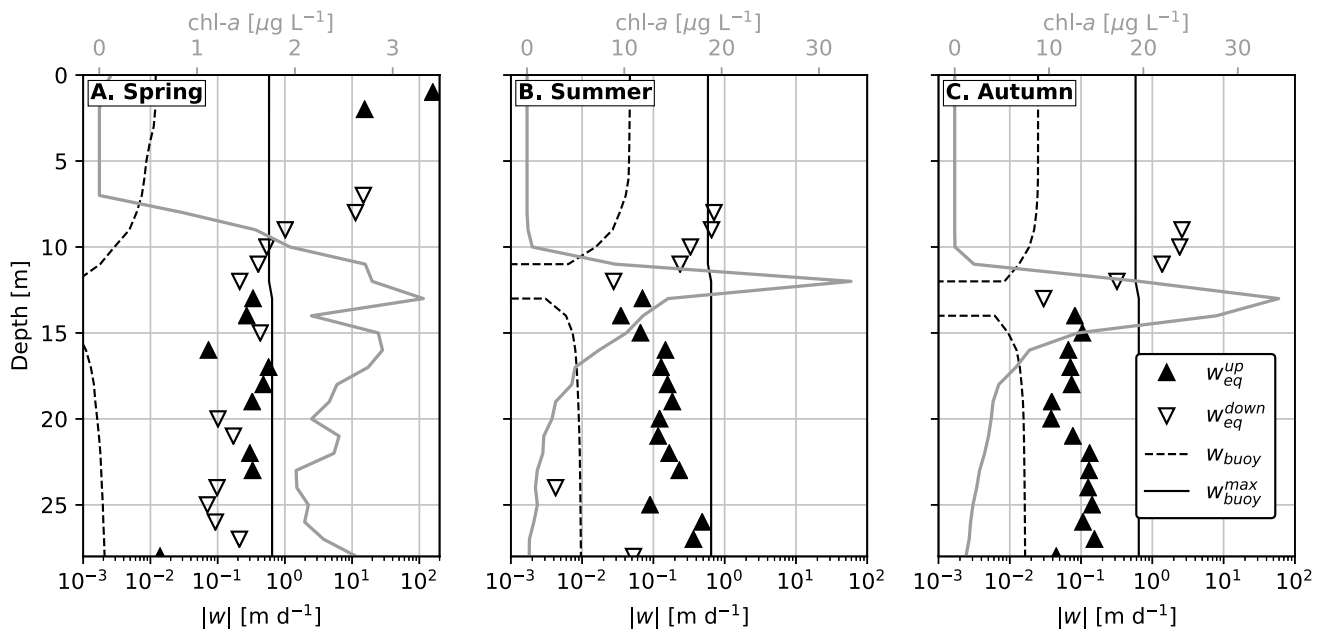


Fig. 10 Vertical velocity (w_{eq} , triangles) required for *P. rubescens* to outcompete turbulent diffusion, as derived from the advection-diffusion balance (Eq. 5). Upward (downward) velocities are shown as filled upward-pointing (empty downward-pointing) triangles. Stokes velocities (w_{buoy}) for *P. rubescens* filaments having their neutral density at the *P. rubescens* peak are shown as black solid lines (i.e. short-term response). Maximum *P. rubescens* stokes velocities

(i.e. long-term response) for maximum/minimum density anomalies ($+27 / -30 \text{ kg m}^{-3}$) observed for *P. rubescens* in lab cultures are shown as dashed lines, positive (resp. negative) anomalies are used above (resp. below) the peak. The *P. rubescens* chl-*a* profile at the beginning of each period is shown in grey. Spring, summer and autumn periods are as defined in Fig. 1

onward as the deepening of the SML progressively eroded stratification. The high summer L_N values indicate that internal wave dynamics in the lake generally follow the linear regime described by Horn et al. (2001) of reduced energy transfer to small scales and reduced mixing. This confirms the interpretation that our microstructure surveys accurately represent summer conditions in Lake Zurich.

Consistent with the seasonal evolution of L_N , spring time measurements gave higher mean basin-scale vertical heat diffusivity (K_T^{BS} , Fig. 9a) below the SML ($\sim 1 \times 10^{-5} \text{ m}^2 \text{ s}^{-1}$) than that estimated for summer and autumn periods ($10^{-6} - 10^{-5} \text{ m}^2 \text{ s}^{-1}$). Mixing was suppressed at $\sim 12 \text{ m}$ depth ($\sim 15 \text{ m}$) during summer and fall. Data from these times gave K_T^{BS} values as low as $1 - 2 \times 10^{-6} \text{ m}^2 \text{ s}^{-1}$. Despite large L_N values during summer months, the metalimnetic basin-scale diffusivity exceeded molecular scales by an order of magnitude. This indicates weak but detectable mixing.

To understand how *P. rubescens* filaments navigate mixing to maintain their vertical position, we compared the vertical restoring velocities that the *P. rubescens* filaments can achieve when displaced from their depth of neutral buoyancy (w_{buoy}), with the velocities required to compensate for dispersion by turbulent mixing (w_{eq}) (Fig. 10). This required an equilibrium velocity that was calculated by integrating

the advection-diffusion equation assuming steady state and zero net growth (Stacey et al. 2007; Steinbuck et al. 2009):

$$w_{eq}(z) = K_T^{BS}(z) \frac{\partial}{\partial z} \left[\ln \left(\frac{C(z)}{C_{max}} \right) \right], \quad (5)$$

where C represents the concentration profile. In this case we used the *P. rubescens* chl-*a* profiles from the bi-weekly monitoring at the beginning of each period (Fig. 1). Figure 9 shows vertical diffusivity profiles used as K_T^{BS} . The restoring velocity represents the balance between buoyancy and drag forces:

$$w_{buoy}(z) = \frac{2gr_s^2(1 - \rho_{fil}/\rho(z))}{9\nu\phi}, \quad (6)$$

where r_s is the equivalent spherical radius of a filament ($\sim 2 \mu\text{m}$; Walsby 2005), ρ_{fil} is the density of the filaments, and $\phi \approx 3.97$ is a form factor for cylindrical filaments. We assumed that for short term perturbations, the density of the filaments equals the density of water at the *P. rubescens* chl-*a* peak. However, laboratory cultures have shown that if the filaments are exposed to higher (lower) light levels for sufficiently long periods of several hours or days, they gain ballast (buoyancy) to a maximum (minimum) anomaly of $\rho_{fil} - \rho = +27 \text{ kg m}^{-3}$ (-30 kg m^{-3}). In this situation, the

restoring velocities would reach maximum values according to Eq. (6) ($w_{buoy}^{max} \approx 0.58 \text{ m d}^{-1}$; Walsby 2005). Here, we will refer to the latter as a long-term response.

For all the periods, the short-term restoring velocities ($w_{buoy} < 0.1 \text{ m d}^{-1}$) fell below the equilibrium velocities (Fig. 10), suggesting that episodic mixing events disrupt the layer on a transient basis. This situation changes when considering the long-term response (w_{buoy}^{max}) indicating that the buoyancy regulation capacity can generally restore the layer after mixing events. In spring, when *P. rubescens* lived below 10 m depth without layer formation, equilibrium velocities of $0.1\text{--}0.5 \text{ m d}^{-1}$ approached but generally fell below restoring velocities (Fig. 10a). This indicates favorable conditions for the *P. rubescens* motility in rising from deeper zones to form the layer. The time-scale for layer formation by buoyancy alone would equate to $\tau \approx (|z_{mean}|/2)/w_{buoy}^{max} \approx 44$ days. This estimate shows good agreement with observations since stratification began at the end of March and the plankton layer was first observed in early May. Vertical migration thus appears to initiate the layer.

In summer and autumn, equilibrium velocities ($w_{eq} \approx 0.1 \text{ m d}^{-1}$) below the layer were several times smaller than w_{buoy}^{max} . This explains the stability of the layer. Equilibrium velocities increased towards the upper edge of the layer in both periods but remained $w_{eq} \lesssim w_{buoy}^{max}$ during summer. In autumn $w_{eq} > w_{buoy}^{max}$, which is consistent with entrainment of the layer by sub-surface mixing.

The role of convective mixing vs. wind mixing

This analysis corroborates direct observations and suggests that metalimnetic mixing driven by internal motions in the interior of the basin or at its boundaries, does not generally reach strengths necessary to overcome *P. rubescens* mobility. Penetration of sub-surface mixing can disrupt the layer from above in autumn when the SML deepens across the metalimnion. Microstructure observations also suggest that, at least at the time of sampling, direct SML wind-driven mixing does not penetrate deep enough to produce entrainment of the *P. rubescens* layer. Nighttime convective mixing however generates overturns large enough to penetrate depths necessary to disrupt the *P. rubescens* layer in autumn. This suggests that convective mixing is responsible for the layer breakdown in autumn.

To assess the generality of this conclusion, we quantified the frequency of conditions favorable for wind and convective entrainment at the base of the SML by comparing the Monin–Obukhov length (L_{MO}) and the SML depth (z_{SML}) (Fig. 9c). When $L_{MO} < 0$, the lake is warming (stable conditions). The reverse applies for lake cooling (unstable

conditions). Wind can potentially produce entrainment in the metalimnion when $|L_{MO}| > z_{SML}$ under either stable or unstable conditions. Fig. 9c shows that conditions for wind-driven entrainment occurred frequently only in late spring (April–June), when the SML was shallow. The frequency of wind-driven entrainment peaked at $\sim 80\%$ in early April. Strong wind events occurred with 20–30% frequency (see figure caption). From June to December $|L_{MO}| > z_{SML}$ events were rare (10% frequency). Over that period, unstable conditions potentially conducive to convective entrainment of the thermocline become more and more prevalent (50% in July to 80% in December). These results indicate that the deepening of the SML in late summer and autumn occurs due to convective mixing and not wind mixing. In summer, the *P. rubescens* layer is located at the core of the metalimnion, $\sim 5 \text{ m}$ below the base of the SML. Entrainment cannot disturb it at this position. Once the SML reaches the top of the *P. rubescens* layer in autumn, however, nighttime convective mixing can entrain the layer and cause its seasonal breakdown.

Comparison with Lake Geneva

Planktothrix rubescens is a widespread species found throughout the world, particularly in perialpine lakes. For those lakes in which *P. rubescens* accumulates as a metalimnetic thin layer in summer, these bacteria become the dominant planktonic species for several years or decades. Lakes Zurich, Hallwil (Stöckli 2012) and Baldegg (Buerger and Stadelmann 2000) in Switzerland, and Lac de Bourget in France (Jacquet et al. 2005) show this trend. However, in Lake Geneva (Switzerland/France), *P. rubescens* occurs only in modest concentrations and mainly during autumn months (CIPEL 2019). Furthermore, *P. rubescens* populations have declined or disappeared in some lakes (i.e., Lac de Bourget, Jacquet et al. 2014), while they remain abundant in others that possess apparently similar nutrient regimes (i.e., Lake Zurich, Posch et al. 2012). To elucidate the reasons behind these differences, Jacquet et al. (2005) analysed a series of bio-physical parameters from two lakes with similar environmental conditions, including a recent history of re-oligotrophication, but also having strongly divergent concentrations of *P. rubescens* (Lac de Bourget and Lake Geneva). These researchers interpreted higher water column stability as contributing to the abundant *P. rubescens* observed in Lac de Bourget.

Here, we extended this comparison between Lake Geneva and Lake Zurich using meteorological and hydrographic data collected in 2018. Wind speeds were generally weaker over Lake Zurich (2.6 m s^{-1}) relative to those affecting Lake Geneva (3.8 m s^{-1}) (Fig. 11a). Bulk water column stability, calculated as the one-dimensional version of the Schmidt stability (Sc' , see caption of Fig. 11) exhibited similar

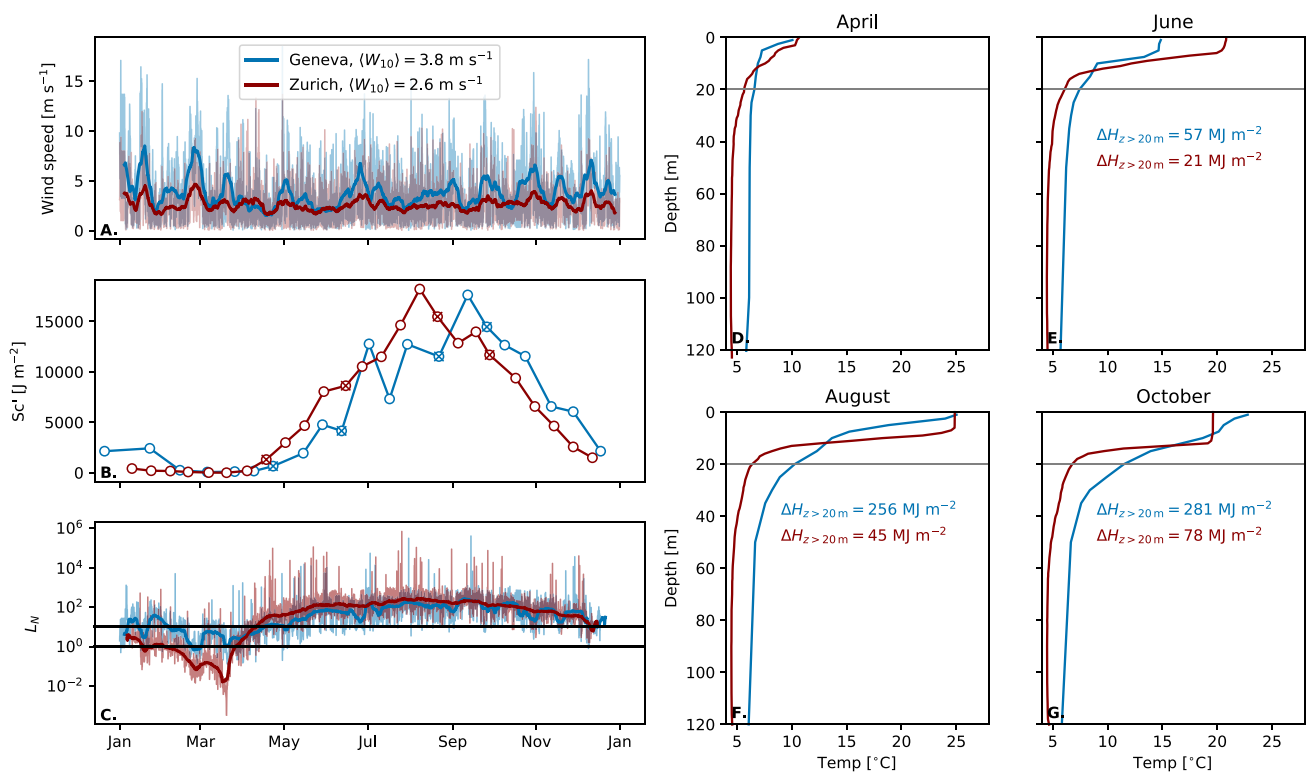


Fig. 11 Comparison of the stratification and mixing dynamics of Lake Zurich (red) and Lake Geneva (blue) during 2018. **a** Hourly and weekly wind speed, **b** one-dimensional Schmidt stability (Sc'), **c** Lake number (L_N) and **d–g** temperature profiles collected in mid-April, June, August and October 2018. The changes in depth-integrated heat content between 20 and 120 m ($\Delta H_{z>20\text{m}}$) with respect to the April profile are shown in **d–g**. Dates of the temperature profiles in **d–g** are marked with a cross in **b**. The datasets used for Lake Geneva are obtained at a single sampling point

maximum summer values but estimates for Lake Geneva showed a delay of more than one month with respect to Lake Zurich (Fig. 11b). These two parameters conferred a different pattern in lake number. Disruptive events ($L_N < 10$) continued to occur regularly over the summer period in Lake Geneva (Fig. 11c) and with relatively high frequency until the end of June. Lake Zurich experienced no disruptive events indicating only weak disturbance of the metalimnion by basin-scale, wind-driven motions.

A series of temperature profiles over the spring–autumn period indicate the different thermal and mixing dynamics for the two systems (Fig. 11d–g). These showed a faster pace of warming and stratification build up in Lake Zurich that became particularly evident in June (Fig. 11e), when Lake Zurich exhibited a warmer epilimnion and more intense metalimnetic stratification. They also suggest that Lake Zurich experiences weaker summer metalimnetic mixing, as indicated by a stronger and thinner thermocline during late summer and autumn months (August, October). The amount of heat accumulated below 20 m over summer also indicates

referred to as SHL2 corresponding to the deepest and pelagic part of the lake. Data were obtained bi-monthly, except for the winter period, for which sampling is performed once a month (Rimet et al. 2020). The one-dimensional Schmidt stability was calculated as $Sc' = -\int_{120\text{m}}^{0\text{m}} g(\rho(z) - \bar{\rho})(z - z_c) dz$. Compared to Eq. (3), here we do not consider the hypsometric function and we stop the integration at the maximum common depth (~ 120 m). This was done to make the values for both lakes comparable (color figure online)

weaker mixing (Fig. 11d–g). This accumulation arises primarily due to turbulent mixing and fell below that observed in Lake Geneva by a factor of three (78 vs. 281 MJ m^{-2}). Metalimnetic mixing ultimately depends on the rate of mechanical energy supplied by the wind estimated as wind work, $P_{10} = \tau W_{10}$ (where τ and W_{10} are wind stress and wind speed at 10 m above the lake surface, respectively; Wüest et al. 2000). The lakes also showed average P_{10} values for the stratified period (April–October) that differed by a factor of three (55 mW m^{-2} vs. 171 mW m^{-2}). This demonstrates a strong link between differences in wind forcing and the intensity of metalimnetic mixing.

Early onset of the metalimnion is also thought to be critical for the formation of the *P. rubescens* thin layer (Yankova et al. 2016). This onset took place more than one month earlier in Lake Zurich than in Lake Geneva due to the faster spring warming in the former. Analysis of a 10-year time-series on lake heat content (Fig. S4) revealed a consistent time-lag of ~ 56 days throughout the time-series confirming this finding. A combination of a stronger thermal inertia

(because of the greater depth) and stronger wind forcing enhance turbulent (latent and sensible) heat fluxes (Fig. S5) to contribute to the observed intensity and duration of winter cooling in Lake Geneva. Lake size and the intensity of wind forcing thus appear to be factors supporting *P. rubescens* growth and development. *P. rubescens* thrives in mid-sized lakes deep enough to sufficiently isolate the metalimnion from surface and bottom enhanced turbulence, but shallow enough so that thermal inertia allows for an early onset of stratification. Mean and maximum depths of lakes Hallwil, Baldegg, Bourget and Zurich fall in intermediate ranges of 28–45 m and 48–145 m, respectively, relative to Lake Geneva which has mean and maximum depths of 155 m and 309 m, respectively.

Conclusions

This study investigated the interaction between vertical mixing and the seasonal persistence (May–October) of an annually recurring thin layer of toxic cyanobacteria (*P. rubescens*) in Lake Zurich using four microstructure surveys and high-resolution mooring deployments. Our measurements revealed that strong metalimnetic stratification inhibits overturning motions and vertical turbulent fluxes which provides a very stable environment for the *P. rubescens* thin layer to form and persist. Comparable sets of measurements available from the oceanographic literature describe similar turbulent environments for a variety of thin plankton layers which frequently appear in association with strong pycnoclines and weakly turbulent or laminar conditions. However, while oceanic features are ephemeral due to frequent disruption by episodic turbulence, weak mixing conditions can persist in Lake Zurich during summer. Our analysis showed that neither entrainment due to surface wind-driven turbulence nor metalimnetic mixing, related to the dissipation of internal lake motions reach the strengths or frequencies necessary to disrupt the layer. This explains its extraordinary seasonal persistence. Instead, the layer breakdown in autumn occurs due to convective deepening of the surface mixed-layer.

A comparative analysis of Lake Geneva, which does not host a *P. rubescens* layer, indicates that low wind forcing (underpinning the weak metalimnetic mixing) and an early onset of stratification (allowed by weak thermal inertia compared to larger lakes) favor the proliferation and stability of *P. rubescens* in the form of a thin layer. These two facts would explain why *P. rubescens* can form thin layers and thrive in medium-sized lakes. Persistent and thin metalimnetic chlorophyll maxima and weak interior turbulent mixing are common features in many lakes. Our results illustrate their connections and underline the relevance of convective

mixing in the seasonal evolution of plankton blooms in stratified waters.

Supplementary Information The online version contains supplementary material available at <https://doi.org/10.1007/s00027-021-00785-9>.

Acknowledgements We acknowledge Sébastien Lavanchy (EPFL) and Michael Plüss (Eawag) for their contribution to the design of the HR-mooring and participation in the field campaigns. We thank Eugen Loher and Daniel Marty for their contribution to the bi-weekly monitoring program. We are grateful to Tomy Doda, Lucas Serra Moncadas, Adem Topak, Camille Minaudo and Luca Cortese for their assistance during fieldwork and MeteoSwiss for the COSMO-1 weather data. This work was financed by the Swiss National Science Foundation Sinergia grant CRSII2_160726 (*A Flexible Underwater Distributed Robotic System for High-Resolution Sensing of Aquatic Ecosystems*), and Grant 200021_179123 (*Primary Production Under Oligotrophication in Lakes*). This study was also supported by the grant *SeeWandel: Life in Lake Constance - the past, present and future* within the framework of the Interreg V-Program Alpenrhein–Bodensee–Hochrhein (Germany, Austria, Switzerland, Liechtenstein) which funds are provided by the European Regional Development Fund as well as the Swiss Confederation and Cantons. The funders had no role in study design, data collection and analysis, decision to publish, or preparation of the manuscript.

Funding Open Access funding provided by EPFL Lausanne.

Compliance with ethical standards

Conflict of interest The authors declare no conflict of interest.

Open Access This article is licensed under a Creative Commons Attribution 4.0 International License, which permits use, sharing, adaptation, distribution and reproduction in any medium or format, as long as you give appropriate credit to the original author(s) and the source, provide a link to the Creative Commons licence, and indicate if changes were made. The images or other third party material in this article are included in the article's Creative Commons licence, unless indicated otherwise in a credit line to the material. If material is not included in the article's Creative Commons licence and your intended use is not permitted by statutory regulation or exceeds the permitted use, you will need to obtain permission directly from the copyright holder. To view a copy of this licence, visit <http://creativecommons.org/licenses/by/4.0/>.

References

- Abbott MR, Denman KL, Powell TM, Richerson PJ, Richards RC, Goldman CR (1984) Mixing and the dynamics of the deep chlorophyll maximum in Lake Tahoe. *Limnol Oceanogr* 29(4):862–878. <https://doi.org/10.4319/lo.1984.29.4.0862>
- Baracchini T, Bärenzung K, Bouffard D, Wüest A (2019) Le Lac de Zurich en ligne - Prévisions hydrodynamiques 3D en temps-réel sur meteolakes.ch. *Aqua Gas - Fachzeitschrift für Gas, Wasser und Abwasser* 99(12):24–29
- Benoit-Bird KJ, Cowles TJ, Wingard CE (2009) Edge gradients provide evidence of ecological interactions in planktonic thin layers. *Limnol Oceanogr* 54(4):1382–1392. <https://doi.org/10.4319/lo.2009.54.4.1382>
- Bluteau CE, Jones NL, Ivey GN (2011) Estimating turbulent kinetic energy dissipation using the inertial subrange method in environmental flows. *Limnol Oceanogr Methods* 9:302–321. <https://doi.org/10.4319/lom.2011.9.302>

- Boegman L, Imberger J, Ivey GN, Antenucci JP (2003) High-frequency internal waves in large stratified lakes. *Limnol Oceanogr* 48(2):895–919. <https://doi.org/10.4319/lo.2003.48.2.0895>
- Boehrer B, Schultze M (2008) Stratification of lakes. *Rev Geophys* 46(2):RG2005. <https://doi.org/10.1029/2006RG000210>
- Bouffard D, Boegman L (2013) A diapycnal diffusivity model for stratified environmental flows. *Dyn Atmos Ocean* 61–62:14–34. <https://doi.org/10.1016/j.dynatmoce.2013.02.002>
- Broullón E, López-Mozos M, Reguera B, Chouciño P, Doval MD, Fernández-Castro B, Gilcoto M, Nogueira E, Souto C, Mouriño-Carballido B (2020) Thin layers of phytoplankton and harmful algae events in a coastal upwelling system. *Prog Oceanogr* 189:102449. <https://doi.org/10.1016/j.pocean.2020.102449>
- Buergi HR, Stadelmann R (2000) Change of phytoplankton diversity during long-term restoration of Lake Baldeg (Switzerland). *Verh Internat Verein Limnol* 27(1):574–581. <https://doi.org/10.1080/03680770.1998.11901300>
- Cheriton OM, McManus MA, Stacey MT, Steinbuck JV (2009) Physical and biological controls on the maintenance and dissipation of a thin phytoplankton layer. *Mar Ecol Prog Ser* 378:55–69. <https://doi.org/10.3354/meps07847>
- CIPEL (2019) Rapports sur les études et recherches entreprises dans le bassin Lémanique. Tech. rep., Conseil Scientifique de la Commission Internationale pour la Protection des Eaux du Léman, Thonon les Bains. ISSN 1010-8432
- Dekshenieks MM, Donaghay PL, Sullivan JM, Rines JE, Osborn TR, Twardowski MS (2001) Temporal and spatial occurrence of thin phytoplankton layers in relation to physical processes. *Mar Ecol Prog Ser* 223:61–71. <https://doi.org/10.3354/meps223061>
- Dillon TM, Caldwell DR (1980) The Batchelor spectrum and dissipation in the upper ocean. *J Geophys Res* 85(C4):1910–1916. <https://doi.org/10.1029/JC085iC04p01910>
- Dillon TM, Park MM (1987) The available potential energy of overturns as an indicator of mixing in the seasonal thermocline. *J Geophys Res* 92(C5):5345–5353. <https://doi.org/10.1029/JC092iC05p05345>
- Durham WM, Stocker R (2012) Thin phytoplankton layers: characteristics, mechanisms, and consequences. *Ann Rev Mar Sci* 4(1):177–207. <https://doi.org/10.1146/annurev-marine-120710-100957>
- Ernst B, Hoeger SJ, O'Brien E, Dietrich DR (2009) Abundance and toxicity of *Planktothrix rubescens* in the pre-alpine Lake Ammersee, Germany. *Harmful Algae* 8(2):329–342. <https://doi.org/10.1016/j.hal.2008.07.006>
- Etemad-Shahidi A, Imberger J (2001) Anatomy of turbulence in thermally stratified lakes. *Limnol Oceanogr* 46(5):1158–1170. <https://doi.org/10.4319/lo.2001.46.5.1158>
- Fink G, Schmid M, Wahl B, Wolf T, Wüest A (2014) Heat flux modifications related to climate-induced warming of large European lakes. *Water Resour Res* 50:2072–2085. <https://doi.org/10.1002/2013WR014448>
- Garneau ME, Posch T, Pernthaler J (2015) Seasonal patterns of microcystin-producing and non-producing *Planktothrix rubescens* genotypes in a deep pre-alpine lake. *Harmful Algae* 50:21–31. <https://doi.org/10.1016/j.hal.2015.10.001>
- Gibson CH (1999) Fossil turbulence revisited. *J Mar Syst* 21(1–4):147–167. [https://doi.org/10.1016/S0924-7963\(99\)00024-X](https://doi.org/10.1016/S0924-7963(99)00024-X)
- Goudsmit GH, Peeters F, Gloor M, Wüest A (1997) Boundary versus internal diapycnal mixing in stratified natural waters. *J Geophys Res C Ocean* 102(C13):27903–27914. <https://doi.org/10.1029/97JC01861>
- Gregg MC (1977) Variations in the intensity of small-scale mixing in the main thermocline. *J Phys Oceanogr* 7(3):436–454. [https://doi.org/10.1175/1520-0485\(1977\)0070436:vltios2.0.co;2](https://doi.org/10.1175/1520-0485(1977)0070436:vltios2.0.co;2)
- Gregg MC (1987) Diapycnal mixing in the thermocline: a review. *J Geophys Res* 92(C5):5249–5286. [https://doi.org/10.1016/0198-0254\(87\)90591-7](https://doi.org/10.1016/0198-0254(87)90591-7)
- Horn DA, Imberger J, Ivey GN (2001) The degeneration of large-scale interfacial gravity waves in lakes. *J Fluid Mech* 434:181–207. <https://doi.org/10.1017/S0022112001003536>
- Imberger J (1985) The diurnal mixed layer. *Limnol Oceanogr* 30(4):737–770. <https://doi.org/10.4319/lo.1985.30.4.0737>
- Imberger J, Patterson JC (1989) Physical limnology. *Adv Appl Mech* 27:303–475. [https://doi.org/10.1016/S0065-2156\(08\)70199-6](https://doi.org/10.1016/S0065-2156(08)70199-6)
- Itswire EC, Koseff JR, Briggs DA, Ferziger JH (1993) Turbulence in stratified shear flows: implications for interpreting shear-induced mixing in the ocean. *J Phys Oceanogr* 23:1508–1522. [https://doi.org/10.1175/1520-0485\(1993\)0231508:TISSFI2.0.CO;2](https://doi.org/10.1175/1520-0485(1993)0231508:TISSFI2.0.CO;2)
- Ivey GN, Imberger J (1991) On the nature of turbulence in a stratified fluid. Part I: the energetics of mixing. *J Phys Oceanogr* 21(5):650–658. [https://doi.org/10.1175/1520-0485\(1991\)0210650:OTNOTI2.0.CO;2](https://doi.org/10.1175/1520-0485(1991)0210650:OTNOTI2.0.CO;2)
- Jabbari A, Rouhi A, Boegman L (2016) Evaluation of the structure function method to compute turbulent dissipation within boundary layers using numerical simulations. *J Geophys Res Ocean* 121(8):5888–5897. <https://doi.org/10.1002/2015JC011608>
- Jacquet S, Briand JF, Leboulanger C, Avois-Jacquet C, Oberhaus L, Tassin B, Vinçon-Leite B, Paolini G, Druart JC, Anneville O, Humbert JF (2005) The proliferation of the toxic cyanobacterium *Planktothrix rubescens* following restoration of the largest natural French lake (Lac du Bourget). *Harmful Algae* 4(4):651–672. <https://doi.org/10.1016/j.hal.2003.12.006>
- Jacquet S, Kerimoglu O, Rimet F, Paolini G, Anneville O (2014) Cyanobacterial bloom termination: the disappearance of *Planktothrix rubescens* from Lake Bourget (France) after restoration. *Freshw Biol* 59(12):2472–2487. <https://doi.org/10.1111/fwb.12444>
- Kraichnan RH (1968) Small-scale structure of a scalar field convected by turbulence. *Phys Fluids* 11(5):945–953. <https://doi.org/10.1063/1.1692063>
- Leach TH, Beisner BE, Carey CC, Pernica P, Rose KC, Huot Y, Brentrup JA, Domaizon I, Grossart HP, Ibelings BW, Jacquet S, Kelly PT, Rusak JA, Stockwell JD, Straile D, Verburg P (2018) Patterns and drivers of deep chlorophyll maxima structure in 100 lakes: the relative importance of light and thermal stratification. *Limnol Oceanogr* 63(2):628–646. <https://doi.org/10.1002/lno.10656>
- Livingstone DM (2003) Impact of secular climate change on the thermal structure of a large temperate central European lake. *Clim Change* 57:205–225. <https://doi.org/10.1023/A:1022119503144>
- Lorke A, Wüest A (2002) Probability density of displacement and overturning length scales under diverse stratification. *J Geophys Res Ocean* 107(C12):3214. <https://doi.org/10.1029/2001JC001154>
- Lorke A, Peeters F, Wüest A (2005) Shear-induced convective mixing in bottom boundary layers on slopes. *Limnol Oceanogr* 50(5):1612–1619. <https://doi.org/10.4319/lo.2005.50.5.1612>
- Luketina DA, Imberger J (2001) Determining turbulent kinetic energy dissipation from Batchelor curve fitting. *J Atmos Ocean Technol* 18(1):100–113. [https://doi.org/10.1175/1520-0426\(2001\)0180100:DTKEDF2.0.CO;2](https://doi.org/10.1175/1520-0426(2001)0180100:DTKEDF2.0.CO;2)
- MacIntyre S, Flynn KM, Jellison R, Romero JR (1999) Boundary mixing and nutrient fluxes in Mono Lake, California. *Limnol Oceanogr* 44(3):512–529. <https://doi.org/10.4319/lo.1999.44.3.0512>
- MacIntyre S, Clark JF, Jellison R, Framb JP (2009) Turbulent mixing induced by nonlinear internal waves in Mono Lake, California. *Limnol Oceanogr* 54(6):2255–2272. <https://doi.org/10.4319/lo.2009.54.6.2255>
- Marti CL, Imberger J, Garibaldi L, Leoni B (2016) Using time scales to characterize phytoplankton assemblages in a deep subalpine lake during the thermal stratification period: Lake Iseo, Italy. *Water Resour Res* 52:1762–1780. <https://doi.org/10.1002/2015WR017200.A>

- Mashayek A, Caulfield CP, Peltier WR (2017) Role of overturns in optimal mixing in stratified mixing layers. *J Fluid Mech* 826:522–552. <https://doi.org/10.1017/jfm.2017.374>
- McManus MA, Alldredge AL, Barnard AH, Boss E, Case JF, Cowles TJ, Donaghay PL, Eisner LB, Gifford DJ, Greenlaw CF, Herren CM, Holliday DV, Johnson D, MacIntyre S, McGehee DM, Osborn TR, Perry MJ, Pieper RE, Rines JE, Smith DC, Sullivan JM, Talbot MK, Twardowski MS, Weidemann A, Zaneveld JR (2003) Characteristics, distribution and persistence of thin layers over a 48 h period. *Mar Ecol Prog Ser* 261:1–19. <https://doi.org/10.3354/meps261001>
- Miles JW (1961) On the stability of heterogeneous shear flows. *J Fluid Mech* 10:496–508. <https://doi.org/10.1143/JJAP.8.821>
- Nash JD, Caldwell DR, Zelman MJ, Moum JN (1999) A thermocouple probe for high-speed temperature measurement in the ocean. *J Atmos Ocean Technol* 16:1474–1482. [https://doi.org/10.1175/1520-0426\(1999\)016<1474:atpfhs>2.0.co;2](https://doi.org/10.1175/1520-0426(1999)016<1474:atpfhs>2.0.co;2)
- Nielsen T, Kiørboe T, Bjørnsen P (1990) Effects of a *Chrysochromulina polylepis* subsurface bloom on the planktonic community. *Mar Ecol Prog Ser* 62:21–35. <https://doi.org/10.3354/meps062021>
- Osborn TR, Cox CS (1972) Oceanic fine structure. *Geophys Fluid Dyn* 3(1):321–345. <https://doi.org/10.1080/03091927208236085>
- Pernica P, Wells MG, MacIntyre S (2014) Persistent weak thermal stratification inhibits mixing in the epilimnion of north-temperate Lake Opeongo, Canada. *Aquat Sci* 76(2):187–201. <https://doi.org/10.1007/s00027-013-0328-1>
- Posch T, Köster O, Salcher MM, Pernthaler J (2012) Harmful filamentous cyanobacteria favoured by reduced water turnover with lake warming. *Nat Clim Change* 2(11):809–813. <https://doi.org/10.1038/nclimate1581>
- Powell T, Jassby A (1974) The estimation of vertical eddy diffusivities below the thermocline in lakes. *Water Resour Res* 10(2):191–198. <https://doi.org/10.1029/WR010i002p00191>
- Preusse M, Peeters F, Lorke A (2010) Internal waves and the generation of turbulence in the thermocline of a large lake. *Limnol Oceanogr* 55(6):2353–2365. <https://doi.org/10.4319/lo.2010.55.6.2353>
- Rimet F, Anneville O, Barbet D, Chardon C, Crépin L, Domaizon I, Dorioz JM, Espinat L, Frossard V, Guillard J, Goulon C, Hamelet V, Hustache JC, Jacquet S, Lainé L, Montuelle B, Perney P, Quentin P, Rasconi S, Schellenberger A, Tran-Khac V, Monet G (2020) The Observatory on LAkes (OLA) database: sixty years of environmental data accessible to the public. *J Limnol* 78(2):164–178. <https://doi.org/10.4081/jlimnol.2020.1944>
- Robertson DM, Imberger J (1994) Lake Number, a quantitative indicator of mixing used to estimate changes in dissolved oxygen. *Int Rev der gesamten Hydrobiol Hydrogr* 79(2):159–176. <https://doi.org/10.1002/iroh.19940790202>
- Ruddick B, Anis A, Thompson K (2000) Maximum likelihood spectral fitting: the Batchelor spectrum. *J Atmos Ocean Technol* 17(11):1541–1555. [https://doi.org/10.1175/1520-0426\(2000\)017<1541:MLSFTB>2.0.CO;2](https://doi.org/10.1175/1520-0426(2000)017<1541:MLSFTB>2.0.CO;2)
- Saggio A, Imberger J (2001) Mixing and turbulent fluxes in the metalimnion of a stratified lake. *Limnol Oceanogr* 46(2):392–409. <https://doi.org/10.4319/lo.2001.46.2.0392>
- Salcher MM, Pernthaler J, Frater N, Posch T (2011) Vertical and longitudinal distribution patterns of different bacterioplankton populations in a canyon-shaped, deep prealpine lake. *Limnol Oceanogr* 56(6):2027–2039. <https://doi.org/10.4319/lo.2011.56.6.2027>
- Schmid M, Köster O (2016) Excess warming of a Central European lake driven by solar brightening. *Water Resour Res* 52:8103–8116. <https://doi.org/10.1111/j.1752-1688.1969.tb04897.x>
- Sepúlveda Steiner O, Bouffard D, Wüest A (2021) Persistence of bioconvection-induced mixed layers in a stratified lake. *Oceanogr, Limnol.* <https://doi.org/10.1002/lno.11702>
- Serra T, Vidal J, Casamitjana X, Soler M, Colomer J (2007) The role of surface vertical mixing in phytoplankton distribution in a stratified reservoir. *Limnol Oceanogr* 52(2):620–634. <https://doi.org/10.4319/lo.2007.52.2.0620>
- Sharples J, Moore MC, Rippeth TP, Holligan PM, Hydes DJ, Fisher NR, Simpson JH (2001) Phytoplankton distribution and survival in the thermocline. *Limnol Oceanogr* 46(3):486–496. <https://doi.org/10.4319/lo.2001.46.3.0486>
- Shih LH, Koseff JR, Ivey GN, Ferziger JH (2005) Parameterization of turbulent fluxes and scales using homogeneous sheared stably stratified turbulence simulations. *J Fluid Mech* 525:193–214. <https://doi.org/10.1017/S0022112004002587>
- Shroyer EL, Benoit-Bird KJ, Nash JD, Moum JN (2014) Stratification and mixing regimes in biological thin layers over the Mid-Atlantic Bight. *Limnol Oceanogr* 59(4):1349–1363. <https://doi.org/10.4319/lo.2014.59.4.1349>
- Smyth WD, Moum JN (2000) Anisotropy of turbulence in stably stratified mixing layers. *Phys Fluids* 12(6):1343–1362. <https://doi.org/10.1063/1.870386>
- Sommer T, Carpenter JR, Schmid M, Lueck RG, Wüest A (2013) Revisiting microstructure sensor responses with implications for double-diffusive fluxes. *J Atmos Ocean Technol* 30(8):1907–1923. <https://doi.org/10.1175/JTECH-D-12-00272.1>
- Stacey MT, McManus MA, Steinbuck JV (2007) Convergences and divergences and thin layer formation and maintenance. *Limnol Oceanogr* 52(4):1523–1532. <https://doi.org/10.4319/lo.2007.52.4.1523>
- Steinbuck JV, Stacey MT, McManus MA, Cheriton OM, Ryan JP (2009) Observations of turbulent mixing in a phytoplankton thin layer: implications for formation, maintenance, and breakdown. *Limnol Oceanogr* 54(4):1353–1368. <https://doi.org/10.4319/lo.2009.54.4.1353>
- Stöckli A (2012) Das Plankton zeigt die Gesundheit des Hallwilersees. *Umwelt Aargau* 58:13–20
- Sullivan JM, Donaghay PL, Rines JE (2010) Coastal thin layer dynamics: consequences to biology and optics. *Cont Shelf Res* 30(1):50–65. <https://doi.org/10.1016/j.csr.2009.07.009>
- Tedford EW, MacIntyre S, Miller SD, Czirkowsky MJ (2014) Similarity scaling of turbulence in a temperate lake during fall cooling. *J Geophys Res Ocean* 119:4689–4713. <https://doi.org/10.1002/2014JC010135>
- Teoh SG, Ivey GN, Imberger J (1997) Laboratory study of the interaction between two internal wave rays. *J Fluid Mech* 336:91–122. <https://doi.org/10.1017/S0022112096004508>
- Thorpe SA (1977) Turbulence and mixing in a Scottish Loch. *Philos Trans R Soc Lond A* 286(1334):125–181. <https://doi.org/10.1098/rsta.1977.0112>
- Walsby AE (2005) Stratification by cyanobacteria in lakes: a dynamic buoyancy model indicates size limitations met by *Planktothrix rubescens* filaments. *New Phytol* 168(2):365–376. <https://doi.org/10.1111/j.1469-8137.2005.01508.x>
- Walsby AE, Schanz F (2002) Light-dependent growth rate determines changes in the population of *Planktothrix rubescens* over the annual cycle in lake Zürich, Switzerland. *New Phytol* 154(3):671–687. <https://doi.org/10.1046/j.1469-8137.2002.00401.x>
- Walsby AE, Ng G, Dunn C, Davis PA (2004) Comparison of the depth where *Planktothrix rubescens* stratifies and the depth where the daily insolation supports its neutral buoyancy. *New Phytol* 162(1):133–145. <https://doi.org/10.1111/j.1469-8137.2004.01020.x>
- Weck J, Lorke A (2017) Mixing efficiency in the thermocline of lakes observed from eddy correlation flux measurements. *J Geophys Res Ocean* 122(1):291–305. <https://doi.org/10.1002/2016JC012188>

- Wiles PJ, Rippeth TP, Simpson JH, Hendricks PJ (2006) A novel technique for measuring the rate of turbulent dissipation in the marine environment. *Geophys Res Lett* 33(21):L21608. <https://doi.org/10.1029/2006GL027050>
- Wüest A, Lorke A (2003) Small scale hydrodynamics in lakes. *Annu Rev Fluid Mech* 35(1):373–412. <https://doi.org/10.1146/annurev.fluid.35.101101.161220>
- Wüest A, Piepke G, Halfman J (1996) Combined effects of dissolved solids and temperature on the density stratification of Lake Malawi. In: Johnson TC, Odada EO (eds) *Limnology, climatology, paleoclimatology East African Lakes*. Climatol, Paleoclimatology East African Lakes, Gordon and Breach, Gordon and Breach, Toronto, pp 183–202
- Wüest A, Piepke G, Van Senden DC (2000) Turbulent kinetic energy balance as a tool for estimating vertical diffusivity in wind-forced stratified waters. *Limnol Oceanogr* 45(6):1388–1400. <https://doi.org/10.4319/lo.2000.45.6.1388>
- Yankova Y, Villiger J, Pernthaler J, Schanz F, Posch T (2016) Prolongation, deepening and warming of the metalimnion change habitat conditions of the harmful filamentous cyanobacterium *Planktothrix rubescens* in a prealpine lake. *Hydrobiologia* 776(1):125–138. <https://doi.org/10.1007/s10750-016-2745-3>

Publisher's Note Springer Nature remains neutral with regard to jurisdictional claims in published maps and institutional affiliations.